JGR Solid Earth

RESEARCH ARTICLE
10.1029/2020JB021195

Chlorine Heterogeneity in Volcanic Glass as a Faithful Record of Silicic Magma Degassing

Shumpei Yoshimura[1] and **Mitsuhiro Nakagawa**[1]

[1]Department of Earth and Planetary Sciences, Hokkaido University, Sapporo, Japan

Key Points:

- We experimentally simulated degassing processes occurring in silicic magma and analyzed Cl content distribution in glass
- The Cl-content distribution was heterogeneous and the distribution pattern was specific to the degassing process experienced
- We analyzed Cl-content in natural silicic lava and revealed that a Cl-rich corrosive gas fluxed and developed permeable flow systems

Correspondence to:
S. Yoshimura,
shumpyos@sci.hokudai.ac.jp

Citation:
Yoshimura, S., & Nakagawa, M. (2021). Chlorine heterogeneity in volcanic glass as a faithful record of silicic magma degassing. *Journal of Geophysical Research: Solid Earth*, *126*, e2020JB021195. https://doi.org/10.1029/2020JB021195

Received 28 OCT 2020
Accepted 22 MAR 2021

Abstract Degassing processes occurring within silicic magma, such as bubble growth, bubble resorption, the welding of magma fragments, and open-system gas loss are crucial in the control of volcanic eruption and lava emplacement, yet their details are still debated. To examine the possibility that these degassing processes are recorded in volcanic glass as heterogeneous Cl distribution patterns, we experimentally simulated these processes by heating rhyolitic obsidian and analyzed the distribution of Cl content in the recovered sample. The results showed that, for bubble growth, Cl diffused toward the bubble interface, leading to Cl depletion around the bubble. For bubble resorption, Cl was discharged from the bubble to the melt, leading to Cl enrichment in the ambient melt. For welding of magma fragments, Cl was depleted near the welded interface because each fragment had degassed Cl at the surface before the welding took place. For open-system gas loss, Cl exsolved at the bubble interface while the bubble itself was being collapsed into a chain of small bubbles and a Cl-depleted tail. These results indicate that Cl distribution is a reliable record of the experienced degassing processes. We then analyzed the Cl distribution in silicic lava from Naruko volcano, Japan, to study the gas flow mechanism. We observed that the glassy matrix was progressively corroded into porous crystalline material. The interface of the glass was highly enriched in Cl. We conclude that a Cl-rich gas fluxed through hot lava and corroded the glass, developing a porous, gas-permeable region.

1. Introduction

Silicic magma erupts in a wide spectrum of styles, ranging from violent explosions that discharge a mixture of high-temperature gas with pyroclasts to non-explosive eruptions that effuse lava gently. Recently, hybrid activity, in which explosive eruption occurs simultaneously with lava dome formation from a common vent, has also been recognized (Castro et al., 2012; Schipper et al., 2013). The variation in eruption style is controlled by degassing processes that occur during magma ascent. As the magma ascends and the pressure decreases, volatile solubility decreases and magma vesiculates. This results in increasing buoyancy and driving eruption forces. In contrast, bubbles interconnect to produce permeable networks resulting in open-system gas loss and a decrease of driving force for eruption (Eichelberger et al., 1986; Gonnermann & Manga, 2007). A shear-induced network of fractures formed within magma may also contribute to the open-system gas loss (Cabrera et al., 2011; Castro et al., 2014; Gonnermann & Manga, 2003; Holland et al., 2011; Kushnir et al., 2017; Saubin et al., 2016; Stasiuk et al., 1996; Tuffen & Dingwell, 2005; Tuffen et al., 2003, 2008). In addition to these processes, bubble resorption and welding of shattered magma fragments may play a significant role in eruption dynamics and formation of dense pyroclasts (e.g., Gardner et al., 2017, 2018, 2019; Rust & Cashman, 2007; Watkins et al., 2012, 2017; Westrich & Eichelberger, 1994)

The abovementioned degassing processes are also important for controlling structural development and self-explosion (explosive disintegration) of hot silicic lava. Silicic lava exhibits a complicated structure composed of the vesicular pumiceous region, dense obsidian region, and crystalline region in a single lava lobe (Fink, 1983; Fink & Manley, 1987). Such structural variation may be produced through gas generation and transport processes (Fink & Manley, 1987; Fink et al., 1992). In addition, silicic lava often causes violent explosions during emplacement because of gas accumulation causing a resultant pressure build-up in bubbles and void spaces. Such explosions are considerably violent and often generate devastating pyroclastic flows and block-and-ash flows (e.g., Castro et al., 2002; Fink & Kieffer, 1993; Navon et al., 1998; Sato et al., 1992).

To understand these degassing-related processes within silicic magma, the chemical heterogeneity of volcanic glass has been extensively investigated. Diffusion profiles of H_2O, CO_2, and semivolatile metals, such

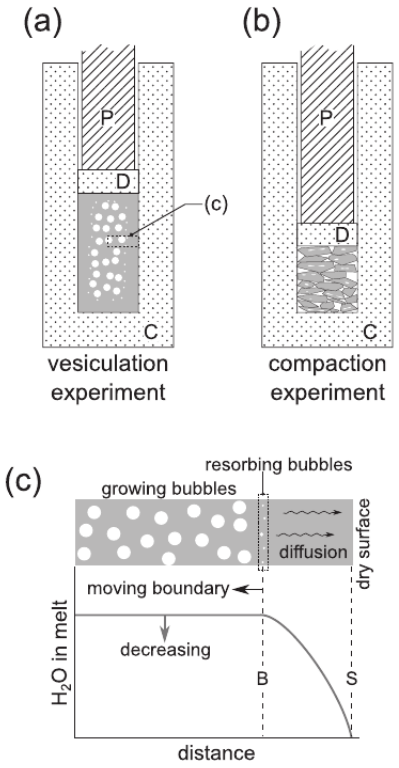

Figure 1. Schematic illustration of (a) the vesiculation experiments and (b) the compaction experiments. C: MgO capsule, D: MgO disk, P: stainless-steel piston. See Appendix A for the entire illustration of the spring-pressuring device. (c) Close-up image of the rectangular area in (a) and the conceptual model of H_2O distribution. "S" denotes the sample surface and "B" denotes the approximate position of the boundary between the bubble-rich region and the bubble-free region. The boundary moves inwards over time as the outermost bubbles resorb.

as Li and ore-forming elements (e.g., Cu, Pb, and Zn), within volcanic glass have been analyzed to estimate timescales of vesiculation (Castro et al., 2005), magma ascent (Watkins et al., 2012, 2017), and gas fluxing through fractures (Berlo et al., 2013; Heap et al., 2019; Paisley et al., 2019; von Aulock et al., 2017). However, the use of diffusion profiles has been limited to samples with low vesicularity where bubble-bubble or bubble-void distances are sufficiently long (a few hundred micrometers) that diffusive heterogeneity can be well characterized. For samples where vesicularity is high and bubble-void distance is short, these volatiles diffuse so rapidly that the heterogeneity is hardly detected. We recently proposed that the Cl-content mapping analysis is useful for investigating the degassing processes of vesiculated lava because Cl has low diffusivity and may be analyzed with a high spatial resolution using an electron probe microanalyzer (EPMA) (Yoshimura et al., 2019). Cl is a major volatile in magmatic systems and partitions into the gas phase as a "passive" component when other major volatiles such as H_2O and CO_2 exsolve (Fortin et al., 2017; Watson, 2017). The occurrence and behavior of Cl are presented by Aiuppa et al. (2009). In silicic volcanoes, a flux of Cl (HCl) gas emission significantly increases during periods of lava extrusion (e.g., Christopher et al., 2010; Edmonds et al., 2008). Cl degassing during magma ascent has not been well theorized because of lack of Cl solubility data under low pressure and low Cl content conditions (conditions of brine undersaturation) (Shinohara, 2009). For Cl diffusivity, recent experiments showed that the Cl diffusivity in silicic melt is much lower than that of H_2O and CO_2, especially under low-H_2O conditions (<1 wt%) (Feisel et al., 2019; Yoshimura, 2018). Therefore, Cl diffusive heterogeneity generated through the shallow-part degassing processes may persist in a vesicular glass without being erased, even after other volatiles are lost or completely homogenized. Yoshimura et al. (2019) actually demonstrated that Cl content was highly heterogeneous in groundmass glass of a rhyolitic lava from Mukaiyama volcano, located in Niijima Island, and proposed a new degassing model regarding the non-explosive eruption of silicic magma.

In this paper, we present a new investigation on Cl degassing in silicic magma. In the first half of this study (Sections 2–5), we experimentally simulated degassing-related processes that may occur in silicic magma: bubble growth, bubble resorption, open-system gas loss, and the welding of magma fragments. Thereafter, we analyzed the Cl-content distribution in the experimental samples and demonstrated that the Cl distribution pattern was specific to each process. This establishes a guide for interpreting Cl-content distribution in a natural silicic glass. In the second half of this study (Section 6), we applied the Cl-content map analysis to a natural silicic lava from the Naruko volcano, Northeast Japan, to investigate the gas flow mechanism within silicic lava. We propose that the Cl content mapping analysis is a promising method to investigate shallow-part degassing of silicic magma.

2. Experimental and Analytical Technique

Two types of experiments were performed to reproduce degassing-related processes occurring in silicic magma. The first experiment was a vesiculation experiment in which the growth and resorption of bubbles were simulated by heating hydrous obsidian (Figure 1). We used this method because it allowed us to observe both bubble growth and resorption in a single experiment, as demonstrated and theorized previously by Yoshimura and Nakamura (2008). The second experiment is the compaction experiment in which obsidian

Table 1
Glass Composition (wt% ± 1σ)

Components	Wada-Pass obsidian	Toyagamori lava, Naruko volcano
SiO_2	76.83 ± 0.08	78.26 ± 0.12
TiO_2	0.08 ± 0.01	0.27 ± 0.02
Al_2O_3	12.58 ± 0.05	11.99 ± 0.06
FeOt[a]	0.54 ± 0.05	1.51 ± 0.05
MnO	0.09 ± 0.03	0.08 ± 0.01
MgO	0.05 ± 0.01	0.28 ± 0.02
CaO	0.53 ± 0.01	1.78 ± 0.03
Na_2O	3.30 ± 0.07	3.85 ± 0.05
K_2O	5.13 ± 0.07	1.66 ± 0.03
Cl	1150 ± 30 ppm	1,070 ± 70 ppm
P_2O_5	not analyzed	0.03 ± 0.02
H_2O[b]	0.75 ± 0.01	0.17 ± 0.01
CO_2[b]	<0.1 ppm	<0.1 ppm
Total[c]	100.00	100.00

[a]Total Fe as FeO. [b]Measured with FT-IR under vacuum. [c]Normalized to 100%.

fragments were uniaxially pressurized at high temperatures (Figure 1b). In this experimental series, both the welding of fragments and open-system gas loss were observed.

2.1. Vesiculation Experiments

Vesiculation experiments were conducted to simulate the growth and resorption of bubbles. Natural rhyolitic obsidian that was collected from a working quarry in Wada Pass, Nagano (Japan) was used as the starting material. The chemical composition of this obsidian was measured with a JEOL JXA-8350f field-emission electron probe microanalyzer (FE-EPMA) at Hokkaido University and is listed in Table 1. The water content of the glass was 0.59 wt% (measured with a micro-FTIR; see Section 2.3). We confirmed that both H_2O and Cl contents were homogeneous throughout the sample by analyzing multiple points of the obsidian. Cylindrical cores (diameter = 4.8 mm, length = 8 mm) were prepared from the obsidian chunk and placed in an MgO cylindrical capsule (inner diameter = 5 mm, length = 13 mm). The capsule was then placed in a stainless-steel pressure vessel, and the obsidian core was pressurized uniaxially with a piston in a spring-pressurizing device under a pressure of 1–3 MPa (Figure 1a; see Appendix A for the entire design of this device). The vessel was then heated at 1000 °C in an electric furnace for 3–24 h. This temperature was chosen because it causes the obsidian to vesiculate immediately. This was essential to study the diffusion behavior of volatiles. The experimental conditions are summarized in Table 2. Note that neither Cl nor H_2O was externally added to the experimental capsule; we focused on volatiles originally dissolved in the obsidian.

During heating, the growth and resorption of bubbles occur in the following, somewhat complicated, manner (Figure 1c). Upon heating, the obsidian immediately softens and vesiculates into a bubbly foam because the initial H_2O content is much higher than the H_2O solubility at 1 atm and 1000 °C. The vesiculated melt soon fills the MgO capsule and the bubbly melt achieves a static condition. Meanwhile, the outer surface of the sample (i.e., the surface melt that is in contact with the MgO) is kept dry and water-undersaturated because the MgO capsule is open (not welded shut). Bubbles near the outer surface therefore resorb into the undersaturated melt, forming a bubble-free region at the margin. The thickness of this bubble-free region increases with time because surface dehydration and the outward water diffusion continue. If the pressure were maintained at a constant level, the inner bubbles would not grow any further after the gas–melt equilibrium is attained. However, preliminary experiments revealed that the pressure gradually decreased and therefore bubbles grew in the following manner. At a certain time in the run, the bubble-free marginal region began to bolster the sample itself against the uniaxial stress, because the viscosity of dry, bubble-free melt significantly increases (to a value of 10^7–10^8 Pa s, as estimated from Giordano et al., 2008). This viscous crust is so rigid that the sample volume is thereafter maintained nearly constant. Because the outermost bubbles continue to resorb while the total sample volume is kept constant, the pressure within the sample gradually decreases, leading to the growth of inner bubbles (the water content in the inner melt also decreases). Therefore, three processes: the dissolution of the outermost bubbles, the decrease in pressure, and the growth of the inner bubbles, proceed simultaneously during heating. A model calculation showed that the pressure decreases to reach approximately 80% of the initial value within 20 h (Yoshimura & Nakamura, 2010). However, despite the complexity and somewhat uncontrolled conditions, the present experiments successfully demonstrated the growth and resorption of bubbles and the associated behavior of Cl.

Table 2
Experimental Conditions

Run#	Temperature (°C)	Initial pressure (MPa)[a]	Heating duration(h)
Vesiculation experiments			
ves07	1000	2.9	7
ves13	1000	1.2	3
ves14	1000	2.9	24
Compaction experiments			
cpt01	900	3.9	6
cpt02	900	4.1	19
cpt03	1000	4.4	6

[a]Estimated from spring length and Hooke's law at the beginning of the experiment (see Appendix A).

2.2. Magma Compaction Experiments

Magma compaction experiments were performed to simulate the welding of magma fragments and open-system gas loss. Obsidian fragments were prepared as the starting material by crushing a chunk of the Wada-Pass obsidian in an iron mortar. The fragments were then sieved to obtain particles of 0.25–1 mm in diameter. Approximately, 100 mg of the sieved fragments was placed into an MgO cylindrical capsule, and they were pressurized uniaxially with the spring-pressurizing device under pressure of ca. 4 MPa (Figure 1b). The vessel was then heated in a furnace at 900–1000 °C for 6–19 h. The experimental conditions are summarized in Table 2. Unlike vesiculation experiments, the pressure in this experimental series was considered to have been constant because no specific structures that could have bolstered the sample against the uniaxial pressure were observed in the experimental sample.

2.3. Analytical Technique

When the time expired, the vessel was quenched in a water bucket. The glassy sample was carefully recovered from the MgO capsule and was cut into two pieces longitudinally. One piece was stored and the other mounted in epoxy and polished to a mirror finish for the optical and electron microscopic observation. For vesiculation experiments, the mean bubble radius was measured by analyzing optical images. Back-scattered electron images (BEIs) were acquired with a JEOL JXA-8350f FE-EPMA at Hokkaido University. Cl-content mapping analysis was performed with the same FE-EPMA with a 100 nA electron beam, 15 kV accelerating voltage, dwell time of 500 ms, and x–y steps of 2 × 2 μm. The map size was typically 0.84 × 0.63 mm (420 steps × 315 steps). Although we used a 2-μm electron beam, the spatial resolution of this mapping analysis is >2 μm because the excitation volume is larger than the beam diameter. For beam calibration, natural and synthetic crystals were used as follows: halite for Cl, SiO_2 for Si, TiO_2 for Ti, Al_2O_3 for Al, Fe_2O_3 for Fe, MnO for Mn, MgO for Mg, wollastonite for Ca, jadeite for Na, and alkali feldspar for K. The Cl count was measured using a PETH crystal, which enabled us to obtain higher count rates (~330%) compared to those of a traditional PET crystal. Following the mapping analysis, the Cl count rate at each point was converted to absolute Cl content based on a calibration line, which was established by comparing the Cl count rate at several points to the absolute Cl content at the same points (Appendix B). The absolute Cl content was determined via standard quantitative analysis; the acceleration voltage and beam current were 15 kV and 10 nA, respectively, and a ZAF correction method was applied. The beam diameter was 2 μm. We note that such a thin beam generally causes significant sodium loss from the glass. However, nearly all of the sodium had already been lost in the 100 nA mapping analysis (which was confirmed by analyzing the map-analyzed portion with a 10-nA, 10-μm defocused beam) and thus no further sodium loss occurred in this 2-μm spot analysis. Cl and K did not show any loss both in mapping analysis and spot analysis. No correction concerning sodium loss was done when measuring the absolute Cl content. When we analyzed starting material, groundmass of lava, and melt inclusions (Section 6), we used a 10-μm, defocused beam to mitigate sodium loss.

For analysis of the H_2O content, we used a JASCO IRT-5200VC Fourier transform infrared spectrometer (FT-IR) installed at Hokkaido University. The glass sample was removed from the epoxy mount that was used for the FE-EPMA analysis and then prepared as a doubly polished thin wafer (thickness was 120–150 μm) such that the FE-EPMA-analyzed surface constituted one side of the wafer (so that the Cl-content distribution could be directly compared with the H_2O-content distribution). The aperture size of the infrared beam was 10 × 10 μm or 20 × 20 μm. For vesiculation experiments, the total H_2O content (OH + H_2O molecule) was determined based on the "species-dependent ε3500 method" developed by McIntosh et al. (2017). We measured absorbances at 3,550 and 1,630 cm^{-1} and calculated OH and H_2O contents by using molar absorptivity from Newman et al. (1986) (55 $L{\cdot}mol^{-1}$ cm^{-1} for H_2O molecules at 1,630 cm^{-1}, 100 $L{\cdot}mol^{-1}$ cm^{-1} for end-member values of OH at 3,550 cm^{-1}, and 56 $L{\cdot}mol^{-1}$ cm^{-1} for end-member values of H_2O molecule at 3,550 cm^{-1}). For the welding experiments, we used a fixed molar absorptivity of 75 $L{\cdot}mol^{-1}$ cm^{-1} (Okumura et al., 2004) to calculate the total H_2O content because the species-dependent ε3500 method was unsuccessful (OH content was negative in all calculations and thus the total H_2O content was not correctly calculated, although all spectra were well shaped). The use of different methods however did not change the conclusion. All FT-IR data are provided in Supporting Information.

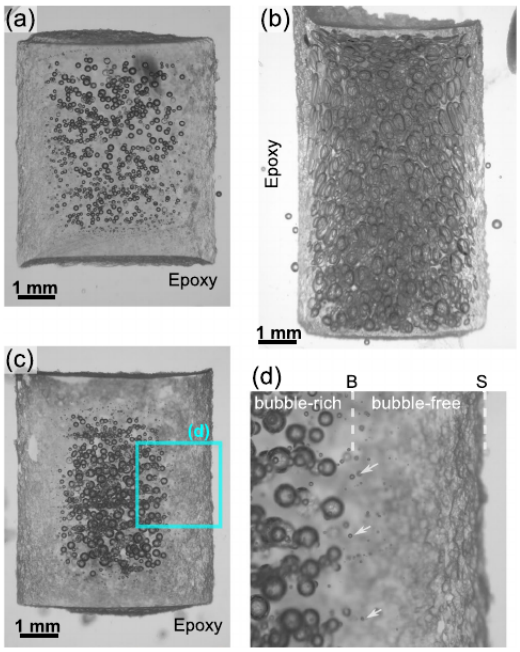

Figure 2. Optical microscopic images of the run products of vesiculation experiments. (a) ves07 (1000 °C, 2.9 MPa, 7 h); (b) ves13 (1000 °C, 1.2 MPa, 3 h); (c) ves14 (1000 °C, 2.9 MPa, 24 h); (d) Close-up view of the rectangular area in (c). All samples showed a structure composed of a bubble-free marginal region and a bubble-rich central region. In (d), "S" denotes the sample surface, and "B" denotes the approximate position of the boundary between the bubble-free region and the bubble-rich region. Bubbles just at the boundary (marked with arrows) are small compared to those in the central region (Table 3), indicating that they are resorbing.

Table 3
Results of Vesiculation Experiments

Run#	H_2O content at central region (wt%)	Final pressure (MPa) (Liu)[a]	Final pressure (MPa) (Duan)[b]	Bubbles in central region (μm)	Outermost bubbles (μm)
ves07	0.51	3.0	8.8	158 ± 27	27 ± 10
ves13	0.41	2.0	7.0	348 ± 79	16 ± 4
ves14	0.49	2.8	8.5	233 ± 70	25 ± 9

[a]Estimated from H_2O content at central region and solubility model of Liu et al. (2005). [b]Estimated from H_2O content at central region and solubility model of Duan (2014) and equation of state by Duan and Zhang (2006).

3. Results

3.1. Vesiculation Experiments

The experimental products of the vesiculation experiments were composed of two distinct regions (Figure 2). The first was a bubble-rich region at the central part of the sample and the second was a bubble-free marginal region. The size of the bubbles was larger and roughly identical within the central region, while the outermost bubbles (bubbles on the boundary between the two regions) were significantly smaller (Table 3). The H_2O content decreased toward the surface of the glass within the bubble-free marginal region, while it was constant within the bubble-rich central region (Figure 3; profile α–β). These results are typical of vesiculation experiments in open systems, in which the outermost bubbles resorb while the bubbles in the central region grow (Yoshimura & Nakamura, 2008). The absence of an H_2O-content gradient between the bubbles (profiles γ–δ, ε–ζ, and η–θ in Figure 3) indicated that the rate of pressure decreases and of bubble growth was sufficiently small that gas–melt quasi-equilibrium was maintained with respect to H_2O. The average rate of pressure decrease can be in principle estimated based on the initial pressure (calculated from spring length and Hooke's law; Appendix A), final pressure (calculated from H_2O content at the bubble-rich central region, and H_2O solubility law), and experimental duration. However, this attempt was unsuccessful because the calculated values of final pressure were higher than the initial pressures with various extent depending on the solubility law used (Table 3).

Figures 4a–4d show the BEIs and Cl-content maps. In the bubble-rich central region, the Cl content decreased toward the bubble interface (profile γ–δ), indicating that bubbles are growing by absorbing Cl (and H_2O) from the nearby melt through diffusion. In contrast, the Cl content near the smaller bubbles (marked with arrows in Figures 4c and 4d) increased toward the bubble interface (profile ε–ζ). This Cl enrichment was the result of bubble resorption. The Cl/H_2O ratio of the gas progressively increases during resorption because H_2O diffuses out by 3–4 orders of magnitude faster than Cl does, meaning that diffusive fractionation occurs (e.g., Watson et al., 2017). The Cl chemical potential of the gas soon exceeds that of the nearby melt, and the Cl begins to diffuse back into the melt.

3.2. Compaction Experiments

Figures 5a–5f show typical BEIs and Cl-content maps of the compaction experiments. In the 900 °C experiments, obsidian fragments were deformed and welded into a glass aggregate (Figures 5a and 5b). The degree of welding varies according to the location; some of the grain interfaces are only partially welded and the original interface is still visible in the BEIs, while others are apparently completely welded and coherent. In addition, various degrees of welding were observed even on a single interface (Figures 3b, 5a and 5b). Such non-uniform welding may indicate that there was local variation in the stress exerted on the contact interface (Quane & Russel, 2005) or surface roughness (Yoshimura & Nakamura, 2010). In the 1000 °C experiment, the obsidian fragments became completely fused and the original interfaces could no longer be identified in the BEI (Figure 5c).

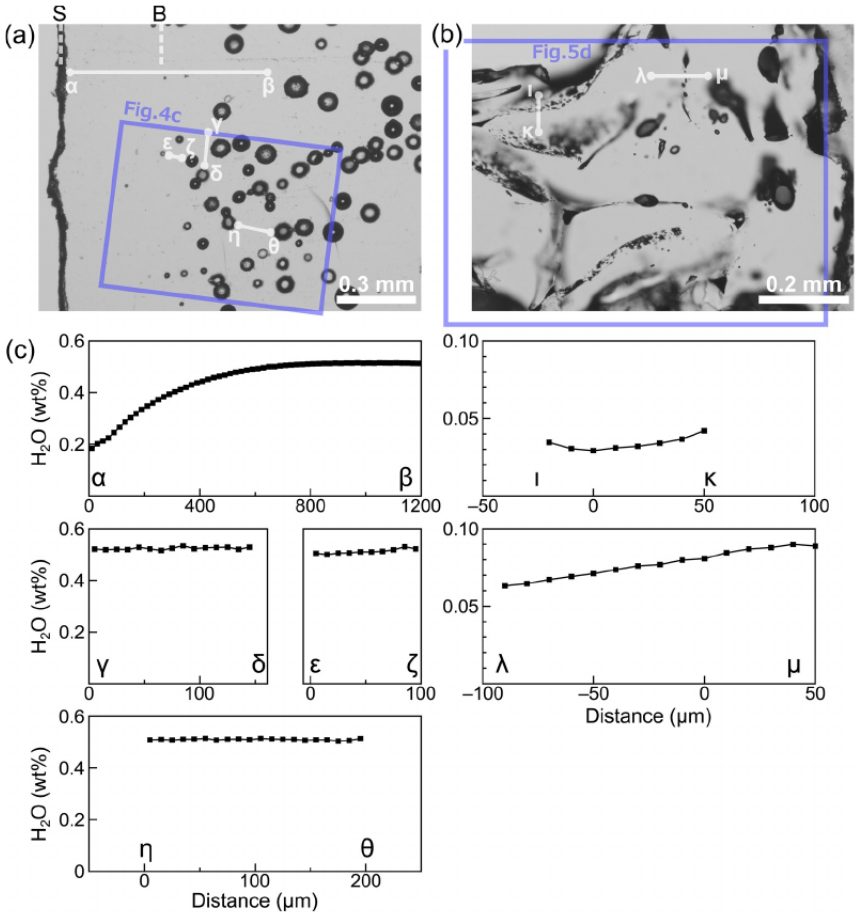

Figure 3. Optical image of the doubly polished glass wafer of (a) the vesiculation experiment (ves07) and (b) the compaction experiment (cpt02). The rectangles indicate the field of the Cl-content maps (Figures 4c and 5d). In (a), "S" denotes the sample surface and "B" denotes the approximate position of the boundary between the bubble-rich region and the bubble-free region. In (b), the interfaces between the obsidian fragments are visible in black dots, because the welding is imperfect and thin spaces are present along the interface. (c) The H_2O content profiles.

In Figures 5d and 5e, the Cl content was significantly low near welded interface compared to that of the inner portion. This indicates that each obsidian fragment had begun Cl degassing at the surface before the fragments were welded into a glass aggregate. The Cl-content profile across a less-strongly welded interface (profile ι–κ in Figures 5d and 5g) was V-shaped and deep, indicating that the interface was still open and the Cl degassing continued. In contrast, the Cl-content profile across an apparently completely welded interface (profile λ–μ) was U-shaped and shallow, indicating that the interface was practically closed and that the profile was under homogenization by diffusion.

An important observation from the magma compaction experiments is that bubbles formed in the melt often showed the shape of a teardrop. An example of this is the two bubbles marked with arrows in Figure 5b. These bubbles are identified as two independent bubbles in the BEI, but they are connected through a Cl-depleted "tail" in the Cl-content map (Figure 5e). This indicates that the two bubbles were originally a large single bubble, which later collapsed into two bubbles under deformation. The Cl content decreased

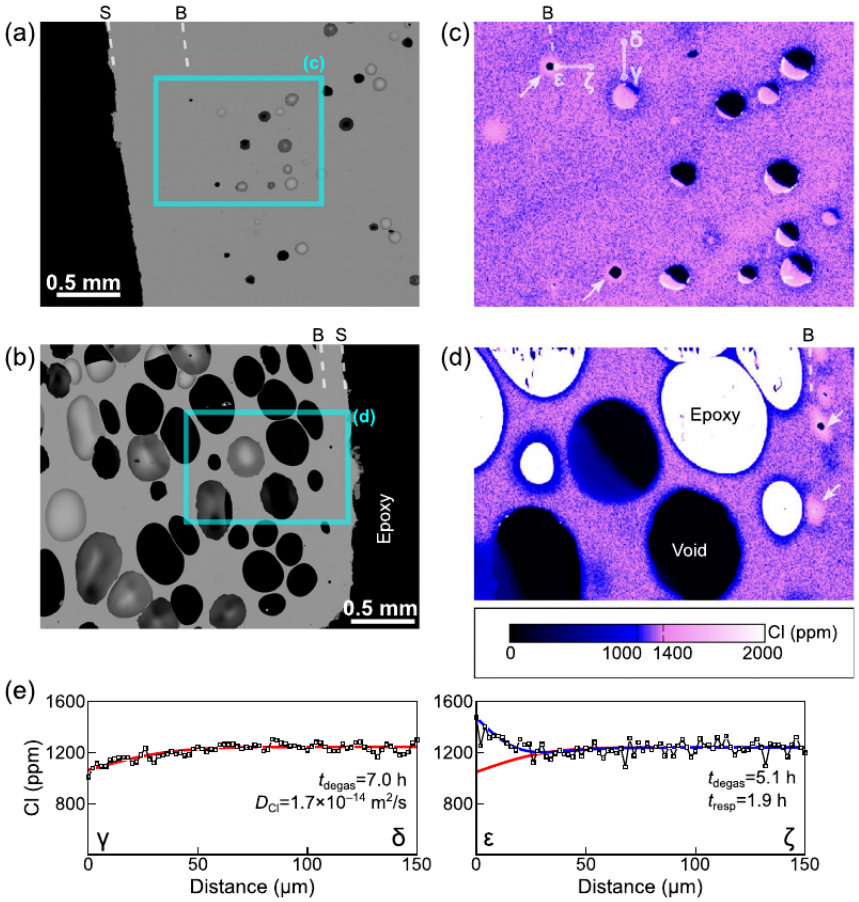

Figure 4. (a and b) BEIs; (c and d) Cl-content maps of the vesiculation experiments. (a and c) ves07 (1000 °C, 2.9 MPa, 7 h); (b and d) ves13 (1000 °C, 1.2 MPa, 7 h). "S" denotes the sample surface and "B" denotes the approximate position of the boundary between the bubble-rich region and the bubble-free region. Arrows in (c) and (d) indicate resorbing bubbles. (e) The Cl-content profiles along the traverses shown in (c). The red line indicates the best-fit profile calculated based on simple diffusion degassing (Appendix C1). The blue line indicates the best-fit profile calculated based on the initial diffusive degassing and the subsequent resorption (Appendix C2).

toward the bubble-melt interface, indicating that gas was exsolving at the bubble interface. The fact that gas exsolution is still occurring while the bubble itself has collapsed indicates that the gas in these bubbles was evacuated to the outside, meaning that the open-system gas loss was occurring. The gas is considered to have escaped in a direction perpendicular to the paper, probably through interconnected bubble channels or a void network between imperfectly welded fragments.

In Figures 5d and 5e, several small spots with high Cl contents were notably observed in the welded glass (marked with arrows). As similar to those observed in vesiculation experiments, these are interpreted as representing the remnants of resorbed bubbles. This resorption is caused due to dehydration of the melt, as was observed in the vesiculation experiments. Bubble resorption due to repressurization (Westrich & Eichelberger, 1994) was unlikely in the present experiments because the pressure of the sample chamber was constant.

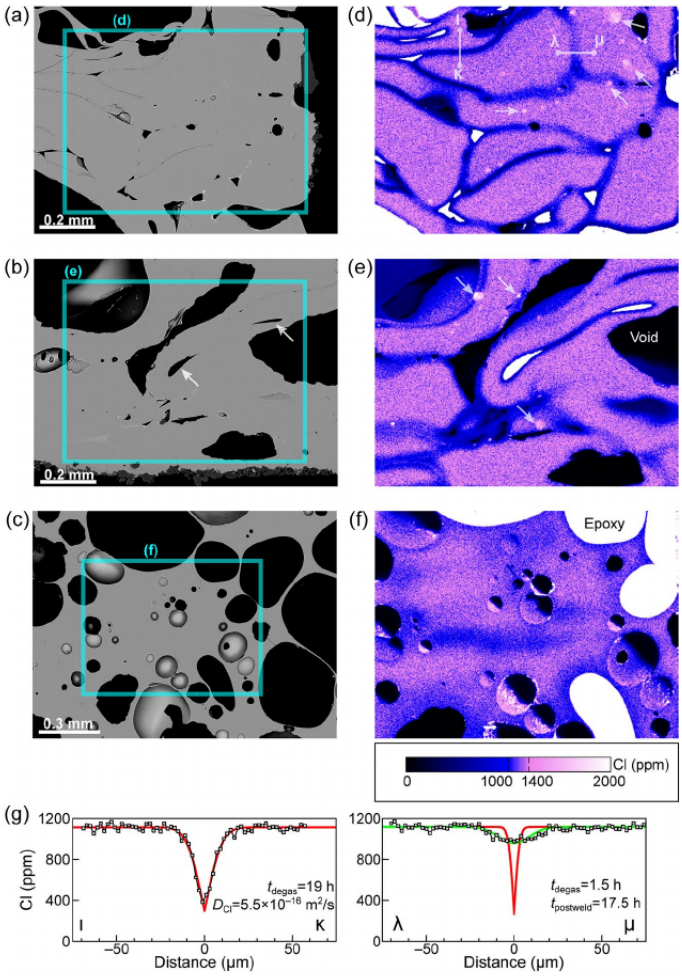

Figure 5. BEIs, Cl-content maps, and Cl-content profiles of the compaction experiments. (a, b, d, and e): cpt02 (900 °C, 4.1 MPa, 19 h), (c and f): cpt03 (1000 °C, 4.4 MPa, 6 h). The white arrows in (d) and (e) indicate the Cl-enriched spots, which represent the remnants of resorbed bubbles. The white arrows in (b) represent drop-shaped bubbles, which had been originally a single large bubble, but later collapsed into two smaller bubbles through open-system gas loss (see Section 3.2). (g) The Cl-content profiles in (d). The red line indicates the best-fit profile that is calculated based on simple diffusion degassing (Appendix C1). The green line indicates the best-fit profile that is calculated based on initial diffusive degassing and the subsequent homogenization after welding (Appendix C3).

4. Discussion

4.1. Vesiculation Experiments

The results showed that the Cl distribution pattern remaining in the glass around a bubble varies depending on whether a bubble is growing or dissolving. If a bubble is growing, then the Cl content decreases toward the bubble interface. If a bubble is resorbing, then the Cl content increases toward the bubble interface. Therefore, Cl-content distribution patterns are used as a new tool to diagnose the behavior of bubbles.

In addition, Cl heterogeneity is useful to estimate timescales (or diffusivity) of related processes through diffusion analysis. For a Cl-content profile near a growing bubble (profile γ–δ, Figure 4e), we used a simple diffusive degassing model (Appendix C1) and estimated the diffusivity to be 1.7×10^{-14} m^2/s. Here, we assumed that this bubble was formed at the beginning of the run and continued diffusive uptake throughout the run (t = 7 h). The obtained diffusivity is consistent with the value that was estimated for 1000 °C by extrapolating the low-temperature (950–650 °C) Cl diffusivity data for rhyolitic melt (Yoshimura, 2018). We then analyzed the diffusion profile around a resorbing bubble (profile ε–ζ, Figure 4e). These bubbles are considered to have had initially grown and then resorbed. Applying a model incorporating initial diffusive degassing and subsequent backward diffusion (Appendix C2) to the profile ε–ζ, and using a Cl diffusivity of 1.7×10^{-14} m^2/s (obtained above), we estimated the timescale of the initial degassing (bubble growth) (t_{degas}) to be 5.1 h and the timescale of resorption (t_{resp}) to be 1.9 h. Here, we fixed $t_{degas} + t_{resp}$ at 7 h (run duration) on an assumption that the bubble was formed at the beginning of the run. The relative error for timescales is considered to fall within ~85% based on the propagation of error of Cl diffusivity (~80%; Yoshimura, 2018) and Dt (~30%). For reference, if the total duration is not fixed at 7 h, then we obtain t_{degas} = 9.3 h and t_{resp} = 2.5 h as the best-fit values.

The Cl distribution in the glass is not necessarily identical to the H_2O-content distribution. Along the profile γ–δ, a clear gradient in Cl was observed around the growing bubbles (Figure 4e), while the distribution of H_2O was homogeneous (Figure 3c). This indicates that a gas–melt quasi-equilibrium was maintained for H_2O because of its high diffusivity (~10^{-11} m^2/s at 1000 °C; estimated based on Zhang & Ni, 2010), while Cl did not attain equilibrium because the diffusivity of Cl is significantly low (~10^{-14} m^2/s at 1000 °C). For resorbing bubbles, H_2O in the gas resorbed into melt and produced a diffusion profile decreasing toward the dry outer surface of the sample (profile α–β in Figure 3c), while Cl was discharged in a short-length scale radially away from the resorbing bubble (profile ε–ζ in Figure 4e). This difference arises because rapid-diffusing, dominant component (H_2O) governed the total behavior of bubble resorption while slow-diffusing Cl was only subordinately concentrated in the gas and resorbed back in the ambient melt.

4.2. Compaction Experiments

Cl diffusive heterogeneity is useful for estimating timescales and the diffusivity of degassing for each glass fragment and its subsequent homogenization after the interface is welded. For a profile across an unwelded interface where diffusive degassing only occurred (profile ι–κ, Figure 5g), we used the simple diffusion model (Appendix C1) and obtained a Cl diffusivity of 5.5×10^{-16} m^2/s. This diffusivity is similar to the Cl diffusivity at 900 °C for dry rhyolitic melt (Yoshimura, 2018). Here, we assumed that the diffusive degassing continued throughout the run (t_{degas} = 19 h). We then analyzed the Cl-content profile across a welded interface where the profile showed a U-shape (profile λ–μ, Figure 5g). Applying a model that incorporates the initial diffusive degassing and subsequent homogenization (Appendix C3) to the profile λ–μ and assuming a diffusivity of 5.5×10^{-16} m^2/s, we estimated that the timescale of the initial degassing (t_{degas}) was 1.5 h and the timescale of subsequent homogenization ($t_{postweld}$) was 17.5 h. Here, we assumed that the total timescale $t_{degas} + t_{postweld}$ was fixed at 19 h because the experimental duration was 19 h for this run. We also assumed that the welding occurred instantaneously at $t = t_{degas}$. The assumption that welding occurs instantaneously within a short duration has been validated in our previous experiments (Yoshimura & Nakamura, 2010). For reference, if the total duration is not fixed at 19 h, then we obtain t_{degas} = 1.9 h and $t_{postweld}$ = 28 h as the best-fit values.

The Cl distribution in the glass is again not necessarily identical to the H_2O-content distribution. Along the traverse ι–κ the H_2O-content profile shows a wide (>50 μm), U-shaped profile, while Cl shows a narrow (~20 μm) V-shaped profile (compare Figure 3c with Figure 5g). Although this difference is mainly due to the difference in diffusivities, we consider that a difference in the spatial resolution of the analytical techniques used (FT-IR vs. EPMA) also contributes to the difference in the shape of the profiles. For the Cl analysis with an FE-EPMA the sample surface was scanned with a 2-μm beam, while for the H_2O analysis with FT-IR, a 10 × 10 μm infrared beam was transmitted through a ca. 120-μm thick wafer. H_2O content was the average value for the ca. 12,000 μm^3 optical path. For the H_2O content profile along the traverse λ–μ (Figure 3c), a monotonic slope was observed while the Cl profile showed a symmetrical U-shape (Figure 5g). This difference may indicate that the interface had been closed off in an earlier stage in the

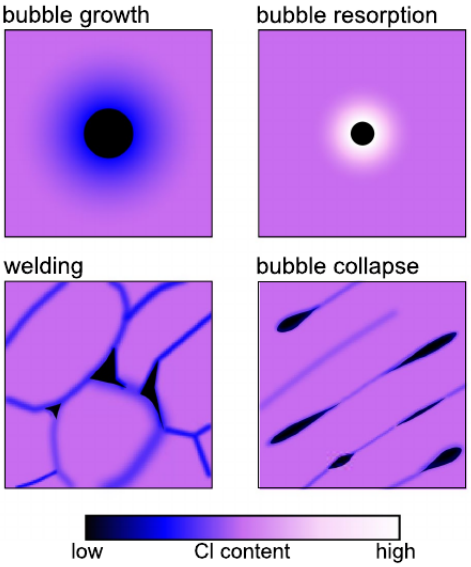

Figure 6. Schematic illustrations of the Cl-content distribution patterns of fundamental degassing processes. For bubble growth, Cl diffused toward the bubble interface, leading to Cl depletion around the bubble. For bubble resorption, Cl was discharged from the bubble to the melt, leading to Cl enrichment in the ambient melt. For the welding of magma fragments, Cl was depleted near the welded interface because each fragment had degassed Cl at the surface before the welding took place. For the open-system gas loss, Cl exsolved at the bubble interface while the bubble itself was being collapsed into a chain of small bubbles and a Cl-depleted tail.

experiment (calculation showed that it is 1.5 h after the onset of heating) and a new boundary condition was established, which soon resulted in a new H_2O distribution. Meanwhile, the Cl continued homogenizing near the welded interface because the change in the boundary conditions did not readily affect the Cl chemical potential distribution because of its low diffusivity.

5. Summary of Experiments and Applicability to Natural Processes

The experimental results demonstrated that the Cl distribution pattern is specific to the process occurring in silicic melt (Figure 6). For bubble growth, the Cl content in the melt decreased toward the bubble interface as a result of diffusive degassing. For bubble resorption, the Cl content was elevated near the bubble interface because the Cl/H_2O ratio of the gas increased as a result of diffusive fractionation, and the Cl diffused back to the melt. For welding of magma fragments, Cl was depleted near the welded interface because each fragment had degassed Cl at the surface before the welding took place. For the open-system gas loss, the bubbles showed signs of both ongoing Cl diffusion toward the bubbles and ongoing compaction of the bubbles. The ongoing compaction was identified as a chain of smaller bubbles with a Cl-depleted tail. These results suggest that the distribution patterns of Cl are useful to explore the degassing processes in both experimental and natural systems.

Cl diffusive heterogeneity was useful to estimate the timescale of the above processes. The range of timescales estimated in the above experiments was a few hours at 900–1000 °C for a diffusion distance of a few tens micrometers. At temperatures typical of natural silicic magma (such as 720–850 °C), the range of Cl diffusion timescales is increased to a few days to a month because the Cl diffusivity decreases by 1–2 orders of magnitude. Therefore, degassing processes occurring in ascending magma, which continues for a few hours or longer during explosive eruption and for a few days to a month during the non-explosive eruption, are suitable targets for this analysis. We caution however that Cl heterogeneity produced through degassing occurring in a deeper part of the conduit tends to be easily erased because Cl diffusivity significantly increases with increasing H_2O content of the melt (Watson, 1991; Yoshimura, 2018). Degassing processes occurring in much shorter time scales, such as degassing of each fragment after magma fragmentation during an explosive eruption, or degassing occurring in much longer duration such as bubble formation in the magma chamber, are inappropriate subjects for this method. Degassing of welded tuff or lava may be well investigated through Cl-content mapping analysis because these processes continue for a long duration under a slowly cooling condition.

6. Application to Natural Silicic Lava

Finally, we investigated the gas flow process occurring within natural silicic lava by applying the Cl-content mapping analysis to Toyagamori lava from the Naruko volcano, located in Northeast Japan. This lava is dacitic to rhyolitic in bulk composition (Ban et al., 2005) and the groundmass glass is rhyolitic (Table 1). The eruption date of this lava is not well known, although it must be younger than 11,800 years (Omoto, 1993). The magmatic temperature has been estimated to be 850 °C based on a magnetite-ilmenite geothermometer (Ban et al., 2005). The interior structure of this lava is partly exposed at several small craters that may have formed through either phreatic explosions that are assumed to have occurred in 837 CE (Tsuchiya et al., 1997) or self-explosions that often occur during emplacement of lava as a result of gas generation and accumulation (Castro et al., 2002; Fink & Manley, 1987). Although the entire lithology of the Toyagamori lava is unclear, this lava exhibits a variety of degassing-related structures, such as vesiculation bandings,

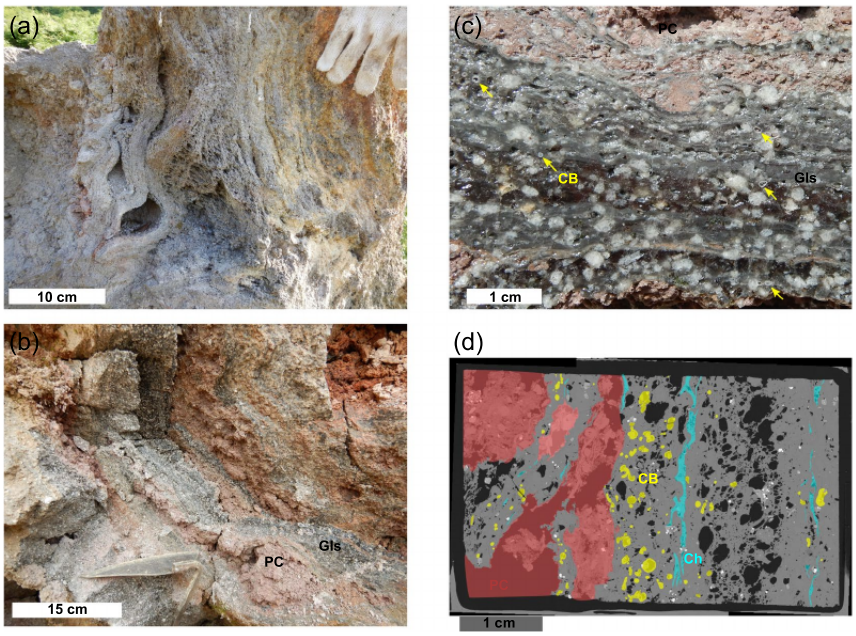

Figure 7. Interior structure of the Toyagamori lava from the Naruko volcano, Japan. (a) Pull-apart layers and gas cavities. (b) Interlayered structure of black glassy region (Gls) and red-gray porous crystalline zone (PC). (c) Close-up view of the cut surface of the Gls–PC interlayer. Arrows show crystal-bearing bubbles (CB). (d) BEI of a thin section. Gray represents the glassy region (glass + plagioclase + quartz) and black represents void space (crystal-free bubble). The colored area represents the porous crystalline region (red), crystal-bearing bubbles (yellow), and bubble channels (cyan).

pull-apart layers, and gas cavities (Figure 7a), offering an exceptional opportunity to study the gas transport mechanisms.

6.1. Results of Textural Observation

The Toyagamori lava typically showed an interlayered structure composed of two contrasting regions: a glassy region where groundmass is composed of bubble-bearing dense glass and a porous crystalline region where groundmass is composed of a mixture of fine-grained crystals, small glass fragments, and pores (Figures 7b and 7c).

6.1.1. Glassy Region

In the glassy region, bubbles with varieties of size and shape were formed in the groundmass. Smaller bubbles are spherical to ellipsoidal in shape, while larger bubbles are more elongated or complicated in form (Figure 7d). The average vesicularity was ~30%, although the spatial distribution of bubbles was heterogeneous. Microlite banding structure (plagioclase and Fe-Ti oxides) was formed along the interlayered structure of the lava. As will be shown in Section 6.2.1, the Cl content of the glass varied from 1,100 to 2,400 ppm depending on location. The H_2O content of glass was 0.18 wt% and was homogeneous at least in a small chip (ca. 2 mm). F and S were not detected in the EPMA analysis.

Bubbles are classified into two types: crystal-free bubbles and crystal-bearing bubbles (Figure 8a–8c, 9a, and 9b). Most bubbles were crystal-free and they had a smoothly rounded glass wall. In contrast, other bubbles contained crystalline material within void spaces. These bubbles (crystal-bearing bubbles) were formed preferentially near the porous crystalline region and bubble channels (the latter will be shown later)

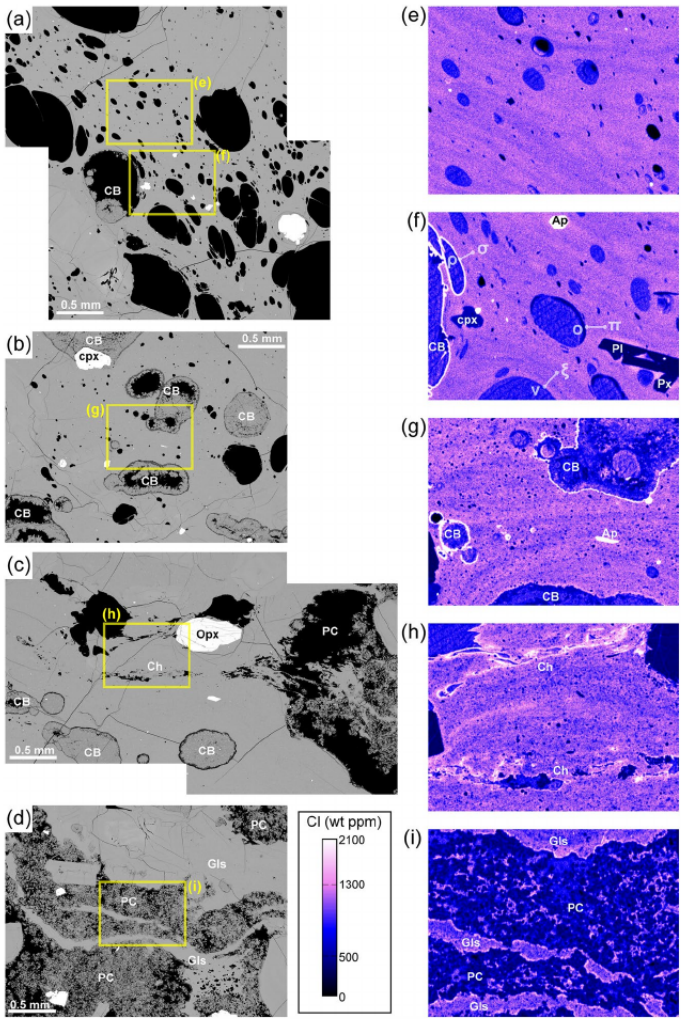

Figure 8. BEIs (a–d) and Cl-content maps (e–i) of the Toyagamori lava. Symbols: Crystal-bearing bubbles (CB), porous crystalline region (PC), bubble channels (Ch), glassy region (Gls), clinopyroxene phenocryst (Cpx), apatite phenocryst (Ap), and plagioclase phenocryst (Pl). A crystal-free bubble is unmarked. Some bubbles were completely occluded with crystalline materials. In the Cl-content maps, it is obvious that the Cl content is highly elevated at the rim of crystal-bearing bubbles and glass edge at the boundary between Gls and PC (f–i). Cl content along the traverses ν–ξ, ο–π, and ρ–σ in (f) is provided in Figure 10.

(Figure 7d). The crystalline material within the crystal-bearing bubble showed a concentric layered structure composed of the outer layer in which acicular to dendritic plagioclase crystals formed a diktytaxitic texture, and the inner layer in which SiO_2 minerals, plagioclase dendrites, and a small amount of Fe-oxide minerals produced an intergrowth texture. At the central void space of the crystal-bearing bubbles, well-shaped prismatic SiO_2 crystals developed (Figure 9a). The average composition of this mineral was SiO_2 = 98.87 wt%, Al_2O_3 = 0.65 wt%, Na_2O = 0.26 wt% (n = 10). Although the phase of this SiO_2 mineral was not determined through spectroscopy, this mineral is most likely cristobalite because it was colorless in

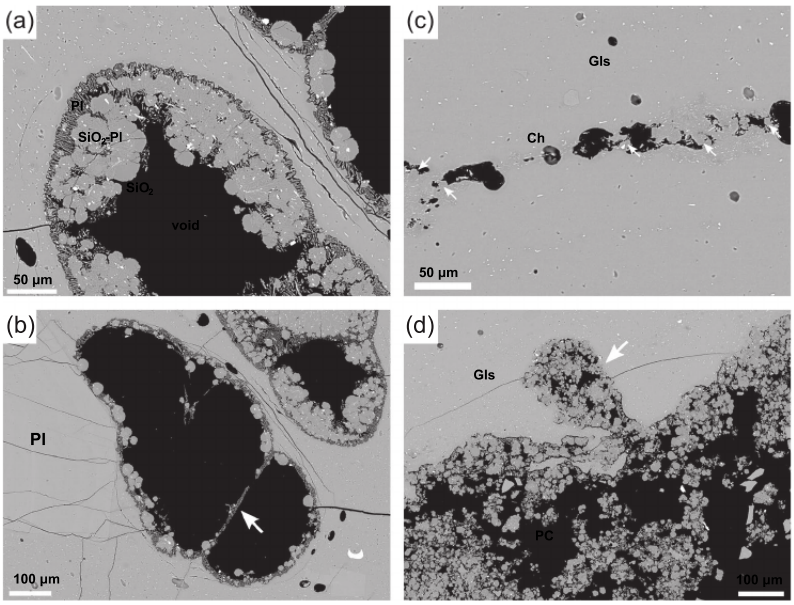

Figure 9. Microscopic texture of the Toyagamori lava (BEIs). (a and b) Crystal-bearing bubbles. Pl: plagioclase diktytaxitic layer; SiO_2: the SiO_2 mineral that is presumably cristobalite; SiO_2–Pl: the layer with SiO_2 mineral–plagioclase graphic texture. Arrow in (b) shows a thin plagioclase diktytaxitic layer, which may have been originally a thin melt (glass) film separating two adjacent bubbles. (c) Bubble channel (Ch) developed in the glassy region. Arrows indicate SiO_2 (most likely cristobalite) and plagioclase crystals, which formed within and along the bubble channel. (d) The boundary between the glassy region (Gls) and the porous crystalline region (PC). Arrow indicates finger-like structure extruding into the glassy region.

plane-polarized light while being dark in cross-polarized light. In addition, fish-scale cracks were formed in some of the larger crystal grains. The wall of these crystal-bearing bubbles was wavy and irregularly curved, rather than smoothly rounded, indicating that the bubble interface was being corroded (Figure 9a). In Figure 9b, it was observed that a thin glass film separating two neighboring bubbles transformed to the material with a diktytaxitic texture, which is identical to the outer plagioclase layer of crystal-bearing bubbles. This observation indicates that the outer plagioclase layer had been originally glassy but later transformed to the plagioclase layer through corrosion reactions (referred to as the corrosion rim).

In the glassy region, chains of small, highly deformed bubbles often formed a channel-like structure (Figures 8c and 9c; hereafter referred to as the "bubble channel"). SiO_2 crystals (again possibly cristobalite) were formed along these channels.

6.1.2. Porous Crystalline Region

The porous crystalline region is red-gray and powdery in hand specimens (Figures 7b and 7c). BEIs show that this region is composed of a mixture of SiO_2 crystals, plagioclase grains, SiO_2–plagioclase intergrowths, a small amount of Fe-Ti oxides (possibly hematite), and thin, unshaped glass fragments (Figures 8d and 9d). The crystals were distributed randomly without forming any specific layered structure. The image analysis demonstrated that the porosity of this region is 52 vol%, and the two-dimensional connectivity, defined as (area of largest interconnected void)/(area of total void) (Nakamura et al., 2008), was 91%, indicating that this region was potentially gas permeable.

BEIs indicate that the boundary between the porous crystalline region and the glassy region was wavy and irregularly curved. In addition, the porous crystalline region formed a finger-like structure intruding into

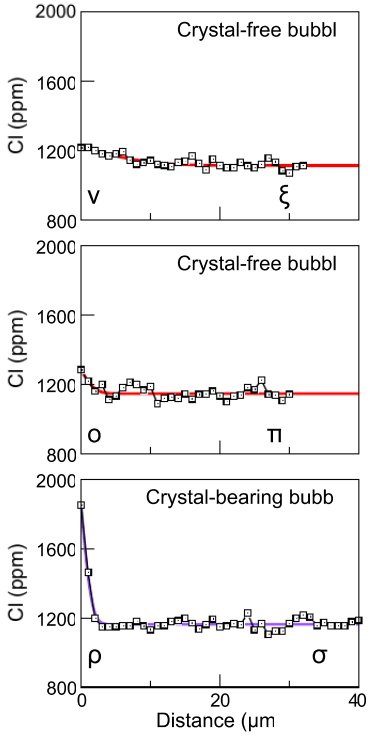

Figure 10. Cl-content profiles around crystal-free bubbles (profile $\nu-\xi$ and $\omicron-\pi$) and crystal-bearing bubbles ($\rho-\sigma$). The position of profiles is shown in Figure 8f. For profiles $\nu-\xi$ and $\omicron-\pi$ Cl-content was weakly enriched at the interface of crystal-free bubbles (high-Cl halo). The timescale obtained through simple diffusion analysis (red curve) was 48 h for profile $\nu-\xi$ and 2.1 h for profile $\omicron-\pi$ (Cl diffusivity is set to 1.7×10^{-16} m^2/s at 850 °C; Yoshimura, 2018). For profile $\rho-\sigma$, the rim of a crystal-bearing bubble was extremely enriched in Cl. Because the interface is progressively destroyed by ongoing corrosion, simple diffusion analysis does not provide any appropriate timescale; If we erroneously apply the simple diffusion model to data (purple curve), then we obtain the timescale of 2.0 h, which is much shorter than the timescale estimated from a thickness of corrosion rim and the corrosion rate (see Section 6.3.3).

the glassy region (Figure 9d). These observations indicate that the glassy region was being corroded and the porous crystalline region extended its "territory".

6.2. Results of Cl-Content Analysis

6.2.1. Glassy Region

The Cl-content maps of the Toyagamori lava showed that Cl distributed heterogeneously in the groundmass glass. In the glassy region, striped patterns with high-Cl contents (1,100–1,300 ppm) and low-Cl contents (1,050–1,150 ppm) were formed in a direction subparallel to the layered structure of the lava (Figures 8e–8h). These Cl-content stripes did not necessarily extend too far afield but were often broken or forked into two bands.

Around crystal-free bubbles, Cl content was slightly elevated compared to that of the low-Cl stripes, forming a high-Cl "halo". This high-Cl halo was blurred and the Cl content decreased radially away from the bubble interface, indicating that Cl is diffusing out of the bubble (Figures 10a and 10b). The width and sharpness of the halo were various; for some bubbles, the halo was well identified while for others the halo was only ambiguously observed. An important observation is that the high-Cl halo was continuously transitioned into a high-Cl stripe. Some bubbles formed at the central part of the high-Cl stripe and others formed at the end of the stripe. These observations indicate that crystal-free bubbles and the Cl-rich stripes were intimately related in origin, as will be discussed later.

For crystal-bearing bubbles, the Cl content was highly elevated at the bubble interface (1,400–2,400 ppm). This extremely Cl-rich rim was different from the high-Cl halo around crystal-free bubbles in that its Cl content was extremely high and that it was discontinuous to the Cl-content striped patterns (Figure 8f). These observations indicate that the crystal-bearing bubbles experienced different (or additional) processes than those of the crystal-free bubbles.

Along the bubble channel, the Cl content was 1,300–2,200 ppm, much higher than that of the Cl content of background groundmass (high- and low-Cl stripes). This Cl-content range overlaps that of the extremely Cl-rich rim around crystal-bearing bubbles (Figure 11).

6.2.2. Porous Crystalline Region

In the porous crystalline region, Cl was only contained in glass fragments (minerals are devoid of Cl). Figure 8i shows that the surface of the individual glass fragment was enriched in Cl compared to the inner portion. In addition, at the boundary between the glassy region and the porous crystalline region, the glass edge was also enriched in Cl. The Cl content at these interfaces and edges is 1,600–1,900 ppm, overlapping with the Cl content of the extremely Cl-rich rim around crystal-bearing bubbles (Figure 11).

6.2.3. Melt Inclusion

We analyzed the Cl content of melt inclusions trapped within quartz and plagioclase phenocrysts to obtain information regarding the initial Cl content within the magma chamber. The Cl content of most of the inclusions was 1,460–2,100 ppm (on average 1,620 ppm; $n = 14$), being much greater than that of the Cl content of background groundmass (high- and low-Cl stripes) but similar to that of extremely Cl-rich rim around crystal-bearing bubbles and Cl-rich glass edges at the boundary of the two regions (Figure 11). F and S were not detected in melt inclusions.

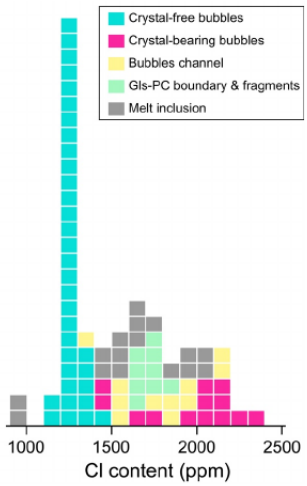

Figure 11. Histogram of Cl-content at the interface (rim) of crystal-free bubbles, crystal-bearing bubbles, the interface of bubble channels, glass edge at the boundary between the glassy region and porous crystalline region, and melt inclusions.

6.3. Discussion

It is widely recognized that cristobalite occurs in void spaces and groundmass of silicic lava. Such cristobalite crystals are considered as a product of either vapor-phase mineralization or devitrification of groundmass glass (e.g., Baxter et al., 1999; Boudon et al., 2015; Horwell et al., 2010, 2013, 2014; Schipper et al., 2015, 2017). According to Horwell et al. (2013), the mechanism of vapor-phase mineralization is subdivided into two extremes: "local redistribution", in which the bubble wall is corroded and minerals precipitated from vapor within the same bubble, and "bulk transport" in which minerals precipitated from deep-derived flowing vapor. Schipper et al. (2015, 2017) showed the three-dimensional structure of cristobalite crystals and pores in bombs from Cordón Caulle and White Island by using X-ray CT and demonstrated that cristobalite was produced in isolated bubbles through the local redistribution. Below we discuss the formation of crystalline materials and gas flow processes in the Toyagamori lava based on the above observations.

6.3.1. Porous Crystalline Region

The key observations regarding the formation of the porous crystalline region include: (1) that the porous crystalline region was highly gas permeable, (2) the boundary between the porous crystalline region and the glassy region was wavy and irregularly curved and finger-like structure was formed, and (3) the Cl content of glass edge at the boundary between the glassy region and the porous crystalline region was extremely high. These facts indicate that a Cl-rich, reactive gas was introduced and flowed through the porous crystalline region, corroding glass interfaces. Thin, unshaped glass fragments in the porous crystalline region may represent the remnant of the original glass. We thus propose that the lava had been originally glassy, but later it transformed into a porous crystalline region through corrosion. The origin of this Cl-rich gas is discussed in Section 6.3.3.

The observation that Cl content was elevated at the interface of bubble channels indicates that the bubble channels represent the infant stage of the porous crystalline region; the Cl-rich gas was introduced in this channel and enlarged the corroded area. The bubble channel may have been formed through shear localization in the flowing lava, as was experimentally demonstrated by Okumura et al. (2010, 2013).

For the formation of porous crystalline texture, we propose that partial leaching of glass and subsequent devitrification were the dominant processes. As the corrosive gas attacked the glass, most of the ions were scavenged to the gas while corrosion-resistant components such as silica and alumina may have preferentially remained. The remaining components may have devitrified into SiO_2 mineral and plagioclase. One supportive observation is the result of Yoshimura (2018), in which rhyolitic obsidian reacted with pure Cl_2 or Cl_2–H_2O gases at 800–950 °C, and a porous SiO_2-mineral layer was formed on the surface of obsidian. However, we note that the gas composition of these experiments was different from that of natural Cl-rich gas. In addition, the mineral assemblage was different (the SiO_2 mineral was only formed in the work of Yoshimura (2018)). Further corrosion experiments under natural magmatic conditions are required to understand the detailed mechanism.

An alternative hypothesis for the formation of the porous crystalline texture is that the glass phase was preferentially scavenged away whilst corrosion-resistant microlites remained. This hypothesis is however eliminated in this work because SiO_2 minerals did not occur as microlite in this lava.

Generally, F plays a significant role in glass corrosion and transport of the silica component (de Hoog et al., 2005). However, we consider that contribution of F is subordinate in the present case because no F was detected in groundmass glass or melt inclusions.

6.3.2. Crystal-Free Bubbles

Important observations for understanding the behavior of crystal-free bubbles include: (1) that the high-Cl halo was formed around these bubbles and (2) that these bubbles seemed to be isolated as they are generally spherical to subspherical in shape and vesicularity is low (~30%). Existence of the high-Cl halo indicates that the Cl content of the gas in these bubbles was elevated after the bubbles were formed. This gas was not however corrosive as evidenced by the smoothly rounded bubble wall. Such Cl enrichment cannot be explained through simple decompressive degassing because the Cl content should decrease, rather than increase, during the degassing (Villemant & Boudon, 1998, 1999). (Note however that some studies showed Cl enrichment in decompressed magma at 50–200 MPa (Gardner et al., 2006; Lukanin, 2015).) We propose that bubble resorption and associated diffusive fractionation are the cause for this Cl enrichment as was demonstrated by experiments (Section 3.1). The fact that the high-Cl halo continuously transitioned into the high-Cl stripes indicates that the bubbles had been deformed and elongated in one direction under dynamic magma flow and then they resorbed, leaving elongated high-Cl stripes. The remaining bubbles then became subspherical to ellipsoidal in shape owing to surface tension when the ambient environment became static (e.g., lava flow ceased). Bubble resorption can be caused by either repressurization (Westrich & Eichelberger, 1994) or melt dehydration. Repressurization may occur if the lava undergoes a conveyor belt motion. Melt dehydration is also likely to occur because the porous crystalline region serves as an open pathway for gas and the water content of nearby melt decreases. The fact that the width and sharpness of high-Cl halo vary depending on bubbles indicates that the timing for the onset of bubble resorption varied, rather than being simultaneous. This is more compatible to melt dehydration because the timing of bubble resorption is various depending upon the distance from the open paths. (We do not confirm any clear relation between Cl enrichment and distance from the paths in two-dimensional images.) If repressurization were the cause, then all bubbles should show a nearly identical extent of Cl diffusion. The possibility that bubble resorption caused by a solubility increase due to cooling (McIntosh et al., 2014) is excluded because the timescale of lava cooling is much longer than that of H_2O and Cl diffusion and no diffusive heterogeneity should remain around bubbles.

The timescale of the resorption of crystal-free bubbles is estimated through diffusion analysis of high-Cl halos surrounding the bubbles. Applying the model of simple one-dimensional diffusion to the profiles, we estimate the timescale to be 1–48 h. This timescale indicates that these bubbles began resorption 1–48 h prior to practical quenching of lava. Note that this timescale is the minimum because temperature gradually decreases in cooling lava. If the temperature is 750 °C, then the timescale increases by an order of magnitude because Cl diffusivity decreases to one-tenth of that at 850 °C.

6.3.3. Crystal-Bearing Bubbles

Crystal-bearing bubbles displayed a rim that was much Cl-richer than those around crystal-free bubbles. This indicates that the crystal-bearing bubbles contained a gas much richer in Cl than the gas in crystal-free bubbles. We examined several scenarios that may explain such Cl enrichment. The first scenario is that this extremely Cl-rich gas was produced through bubble resorption, similar to Cl-rich gas in crystal-free bubbles. This scenario is however excluded because such Cl enrichment can be accomplished only when resorption proceeded to such a high extent that these bubbles become much smaller than crystal-free bubbles. This is inconsistent with the observation that size of crystal-bearing bubbles is apparently similar to crystal-free bubbles (Figure 7d). The second possibility is that crystal-bearing bubbles were formed in an earlier stage and thus contained a Cl-rich gas while crystal-free bubbles were formed in a later stage from a Cl-depleted melt. This possibility is also excluded because if this were the case, then crystal-bearing bubbles should be significantly larger than crystal-free bubbles. The third possibility is that the Cl content of the bubble increased as a result of microlite crystallization of nearby melt (as similar to the idea of Schipper et al., 2017; see discussion presented later in this section). This possibility is excluded because the type of bubbles (crystal-free or -bearing) seems to be unrelated to microlite crystallinity. The final possibility is that the extremely Cl-rich gas was imported from the porous crystalline region. This possibility is supported by several observations. First, crystal-bearing bubbles exist preferentially near the porous crystalline region and bubble channels. Second, the Cl content of the extremely Cl-rich rim around the crystal-bearing bubbles overlaps the Cl content of the glass edge at the boundary between the glassy region and the porous crystalline region

(and interface of glass fragments in the porous crystalline region) (Figure 11). These observations suggest that Cl-rich gas in the porous crystalline region corroded glass and flowed into nearby bubbles. However, an inlet of the gas is at present unidentified; in two-dimensional images, most of the bubbles seem to be isolated and no pathway is formed between the bubble and porous crystalline region. We propose that the inlet was a small, tiny hole produced through corrosion and it is rarely observed in two-dimensional images. This idea should be examined in three-dimensional space based on X-ray CT.

Once the extremely Cl-rich gas was introduced into a bubble, the gas began corrosion of bubble wall and formation of crystalline materials. Existence of the concentric layered structure indicates that the crystalline material precipitated from a stagnant gas in a calm environment, most likely in a local-redistribution manner; if the gas were vigorously flowing in these bubbles and the bulk transport was dominant, then such a layered structure would not be produced as in the case of the porous crystalline region. To maintain a stagnant environment, the gas inlet must be narrow enough to block turbulent gas transfer from the porous crystalline region. This is again consistent with the fact that the inlet is rarely seen in two-dimensional images. To strictly confirm whether local redistribution was dominant, a mass balance calculation involving chemistry of corrosion rim and background groundmass is necessary (Schipper et al., 2015).

The timescale of corrosion (and formation of crystalline materials) is difficult to estimate through Cl diffusion analysis because the Cl diffusion profile around crystal-bearing bubbles is progressively destroyed by ongoing corrosion. To strictly calculate the timescale, a moving-boundary diffusion model involving surface reaction is necessary. However, for rough, first-order estimation, it is convenient to compare the corrosion rate and thickness of the corrosion rim (diktytaxitic layer). The thickness of the corrosion rim was typically 10–30 μm. For the corrosion rate, because systematic data at magmatic temperatures are non-existent, we tentatively use the value of 0.3 μm/h, which was obtained in reaction experiments of rhyolitic obsidian in Cl-rich gases at 850–950 °C (Yoshimura, 2018). Using these values, we determined the timescale to be 100–300 h. Interestingly, this timescale is similar to the previous estimation by Schipper et al. (2015, 2017) in which 10 μm corrosion rims could be produced in hours to days, although Schipper used a low-temperature corrosion rate because of lack of data at magmatic temperatures. For further understanding of corrosion mechanism, corrosion experiments under realistic magmatic temperatures and gas compositions should be necessary.

It must be noted that the above scenario concerning the origin of crystal-free and -bearing bubbles is inconsistent with (or opposite to) the work of Schipper et al. (2015, 2017), in which crystal-bearing bubbles are isolated while crystal-free bubbles are interconnected. Schipper et al. (2017) showed that the Cl content of residual melt in groundmass was higher than that of melt inclusion and proposed that the gas in bubbles became Cl-rich as a result of microlite crystallization associated with closed-system degassing. This gas then corroded the bubble wall and precipitated cristobalite in a local-redistribution manner. However, a completely different scenario, in which isolated bubbles resorbed and increased the Cl content of the gas because the water content of glass decreased through diffusive degassing toward interconnected bubbles (open-system pathway), is also applicable. Because these authors only presented the average Cl content of most evolved parts of interstitial glass and did not show the location of an analyzed point, it is hard to further discuss whether and how the Cl-rich gas was produced.

6.3.4. Origin of Cl-Rich Corrosive Gas

The origin of Cl-rich gas flowing through the porous crystalline region is presently unidentified. Simple decompressive degassing of the magma cannot produce such a Cl-rich gas because the Cl content of both melt and gas should decrease significantly from the original value during degassing (Villemant & Boudon, 1998, 1999). An alternative scenario is that the Cl-rich gas originated from the magma chamber. The gas stored in the magma chamber ascended through magma in the volcanic conduit (through a permeable network of interconnected bubbles or shear-induced fractures) and then laterally flowed to the distal part of the lava. This possibility is proposed because the Cl-content range of melt inclusion (1,460–2,100 ppm) overlapped that of extremely Cl-rich rim around crystal-bearing bubbles, the interface of bubble channels, and Cl-rich edge at the boundary between glassy and porous crystalline regions (Figure 11).

However, the production mechanism of Cl-rich corrosive gas is a future issue dealt with by detailed Cl solubility law.

6.3.5. Entire Scenario

Finally, we propose the following scenario based on the presented observations and considerations (Figure 12). The Toyagamori lava was initially glassy and basically gas impermeable at the initial stage of emplacement. Bubble channels have been formed only locally (possibly because shear localization occurred in the flowing lava) and the gas permeability was elevated at these channels. An extremely Cl-rich gas, which possibly originated from a magma chamber, was then introduced into the lava and flowed through the bubble channel. Because of its high reactivity, Cl-rich gas corroded the glass and transformed it into the porous crystalline region. The porous crystalline texture was formed through partial leaching of glass and subsequent devitrification. As the corrosion occurs, Cl-rich gas was introduced to nearby closed bubbles through corrosion-induced tiny holes on the bubble wall. The inner wall of these bubbles was corroded and the interface became wavy. The scavenged components precipitated within the same bubble in a local-redistribution manner and formed concentric-layered crystalline materials. This has begun 100–300 h prior to practical quenching of the lava. In the meantime, bubbles far from the porous crystalline region maintained the closed system and contained the original Cl-poor gas. However, these bubbles began resorption because the water content of the nearby glass decreased through diffusive degassing toward the porous crystalline region. This resorption started 1–48 h prior to practical quenching of lava. During resorption, the glassy region had been flowing dynamically, as is evidenced by the existence of high-Cl stripes.

In the above scenario, the corrosive nature of the Cl-rich gas plays a significant role in the development of lava structure. As glass is corroded by the Cl-rich gas, the permeability of the lava increases. Once the permeability increases, a greater amount of the corrosive gas is introduced and the permeability further increases. Because of this positive-feedback effect, the gas-flow system in the lava may develop rapidly. The gas in the lava may be released smoothly to the outside because of its high permeability. This reduces excess gas pressure in void spaces and thereby prevents the self-explosion of lava.

The above idea could be applied to the gas flow process occurring within ascending magma. If a Cl-rich gas stored in a magma chamber flows through ascending magma, then fluid-mobile elements in melt near the gas pathway are scavenged. This process changes melt composition (alkali loss, Webster & Holloway, 1988) and possibly induces crystallization, increasing magma viscosity. Therefore, the gas pathway may be maintained for extended durations and allows further gas escape. We thus propose that corrosion is a new mechanism to promote open-system gas loss and weaken the explosivity of a gas-rich magma.

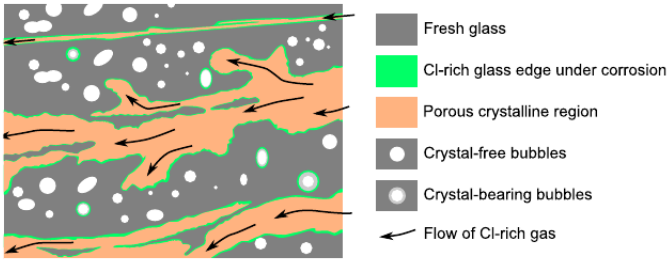

Figure 12. Model of gas flow and corrosion of glass within silicic lava. The Cl-rich gas flows through pre-existing pathways such as bubble channels and corrodes glassy wall, increasing the total permeability. This allows for the introduction of a greater amount of gas into the lava, further increasing permeability. Owing to this positive-feedback effect, the interior structure of the lava may develop rapidly.

Appendix A: Spring-Pressuring Device

Figure A1a shows the spring-pressurizing device used in this study. The MgO capsule (C) containing sample (S) was placed in the stainless-steel pressure vessel (V). A thin MgO disk (D) was placed on the top of the sample so that the stainless-steel piston (P) did not touch the sample directly. The pressure is generated through the tension of two springs (Sp). Displacement of the springs can be adjusted by rotating the supporting nut (N) around the screw-threaded part of the piston. The pressure exerted on the top of the sample was calculated based on the spring length-pressure relationship (Figure A1b).

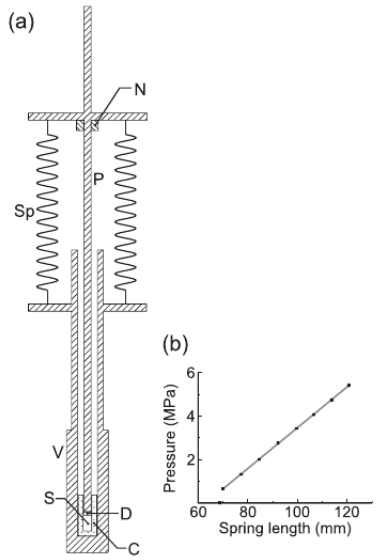

Figure A1. (a) Schematic image of the spring-pressuring device. C: MgO capsule, D: MgO disk, N: nut used for adjusting the pressure (spring elongation). P: stainless-steel piston (upper part is screw-threaded), S: Sample space, Sp: Iron wire spring, V: stainless-steel (SUS304) pressure vessel (composed of a bolt and long nut). (b) Spring length–pressure relation for the spring "SR-2135". A linear relation (Hooke's law) is confirmed except in the range 65–70 mm.

Appendix B: Calibration Line for Converting Cl Count to Concentration

We established a calibration curve to convert the Cl intensity at each point of the analyzed map to absolute Cl content. We assumed that a linear relationship exists between the Cl intensity and absolute Cl content. Applying a fitting calculation to the data, we obtained Cl (ppm) = 8.93 (±0.39) × c−295.7 (±60.3) for Wada-Pass obsidian (Figure B1a) and Cl (ppm) = 5.75 (±0.42) × c + 253.5 (±69.7) for Toyagamori lava (Figure B1b). Here, c represents counts per 500 ms for Cl obtained using a PETH crystal and 100 nA beam. The gradient and intercept of the equation are different between the samples, which may have arisen because of the difference in glass composition (matrix effect).

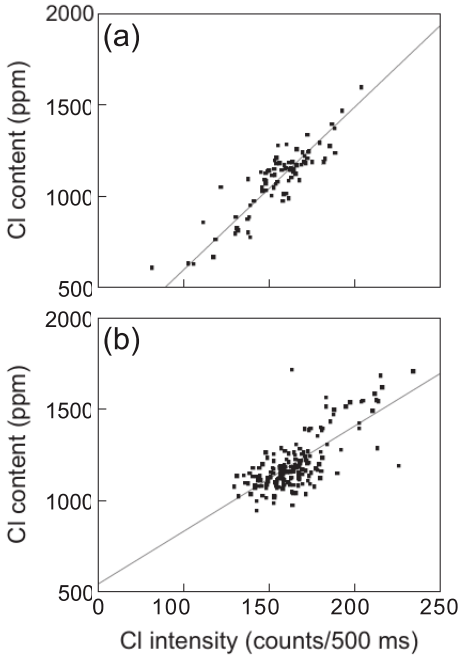

Figure B1. Calibration lines were used to convert the Cl count rate to absolute concentration for (a) Wada-Pass obsidian and (b) Toyagamori lava.

Appendix C: Calculation of Timescales Based on Cl Diffusive Heterogeneity

To calculate the timescales of bubble growth and resorption, it is reasonable to solve the bubble-growth equations constructed in a polar coordinate system while taking the moving boundary effect into account (e.g., Proussevitch & Sahagian, 1996). However, for simplicity, we used one-dimensional equations in a semi-infinite medium without considering the moving boundary effect. Such simplification may result in large inaccuracies in the calculation, but this is not a significant disadvantage in terms of demonstrating the usefulness of Cl diffusion for calculating the timescales. For the degassing and welding at the surface of the obsidian fragments, the one-dimensional simple model is more realistic because the surface of the fragment is relatively flat.

C1. Diffusive Degassing Model

The Cl diffusion in a semi-infinite medium is described by (Crank, 1975):

$$C = C_{\text{boundary}} + \left(C_{\text{initial}} - C_{\text{boundary}}\right)\text{erf}\left(\frac{x}{2\sqrt{Dt}}\right) \tag{C1}$$

where C is the concentration, D is the Cl diffusivity, t is the time, and x is the distance from the interface. The subscript "initial" represents the Cl content before diffusion, and "boundary" represents values at the bubble interface or at the surface of an obsidian fragment. Dt, C_{boundary}, and C_{initial} were determined simultaneously by fitting Equation C1 to the observed Cl-content profiles. D (when the experimental duration is given) or t (when diffusivity is assumed) was then determined. The resulting value of Dt typically has an error of 30% relative.

C2. Diffusive Degassing and Bubble Resorption Model

For bubble resorption, we assume that the bubble initially grew by taking up Cl (and H_2O) from the nearby melt and then turned to resorb when the surrounding melt became water-undersaturated. We thus assumed that Cl diffusive degassing first occurred during the period of $0 \le t \le t_{degas}$ and then backward Cl diffusion (resorption) followed during $t_{degas} \le t \le (t_{degas} + t_{resp})$. Here, t_{degas} and t_{resp} represent the timescale of diffusive degassing and resorption, respectively. For this calculation, we numerically solved the original form of the one-dimensional diffusion equation using the finite difference method:

$$\frac{\partial C}{\partial t} = D\frac{\partial^2 C}{\partial x^2} \tag{C2}$$

At $0 \le t \le t_{degas}$, Equation C2 was solved under the initial conditions of $C\,(t = 0) = C_{initial}$ and boundary conditions of $C\,(x = 0) = C_{boundary}$. For $C_{initial}$, the average content at the plateau of the Cl-content profile was used. For $C_{boundary}$, because it was difficult to estimate its value from the observed Cl profile, we instead used the value of $C_{boundary}$ that was obtained from the simple diffusion model (Appendix C1) and the Cl-content profile of nearby growing bubble. At $t = t_{degas}$, the boundary condition was changed to $C\,(x = 0) = C_{boundary\text{-}high}$ ($C_{boundary\text{-}high} > C_{boundary}$) to cause backward diffusion (resorption). Here, note that we assumed that the change from growth to resorption coincides with the change in the Cl boundary conditions at $t = t_{degas}$, although there is actually a small time delay between those two events because the increase in the Cl/H_2O of the gas through diffusive fractionation takes some time. The value of $C_{boundary\text{-}high}$ was set to the Cl content near the interface of the resorbing bubble. Equation C2 was further solved until $t = t_{degas} + t_{resp}$. By testing all possible combinations of t_{degas} and t_{resp}, we determined the Dt_{degas} and Dt_{resp} such that the calculation profile best fits the observed data. t_{degas} and t_{resp} were then determined using the value of D that was pre-determined by applying the simple diffusion model (Appendix C1) to a Cl-content profile near a growing bubble.

C3. Diffusive Degassing and Welding Model

For the welded interface of an obsidian fragment or the bubble walls in a natural lava, it is considered that the diffusive degassing initially occurs to produce a V-shaped profile across the interface, after which the interface was welded and the profile was being homogenized to a U-shaped. We assumed that the initial diffusive degassing toward the interface occurred at $0 \le t \le t_{degas}$, and that diffusive homogenization followed at $t_{degas} \le t \le (t_{degas} + t_{postweld})$. Here, t_{degas} is the timescale of the diffusive degassing and $t_{postweld}$ is the timescale for the homogenization after welding. Note that we assumed that welding occurs instantaneously at $t = t_{degas}$. This assumption is valid, as was confirmed in the fracture healing experiments of Yoshimura and Nakamura (2010). At $0 \le t \le t_{degas}$, Equation C2 was solved numerically under the initial condition of $C\,(t = 0) = C_{initial}$ and the boundary condition of $C\,(x = 0) = C_{boundary}$. For $C_{initial}$, we used the average content at the plateau of the Cl-content profile. For $C_{boundary}$, because it was difficult to estimate its value from the observed Cl profile, we instead used the value of $C_{boundary}$ that was obtained from the simple diffusion model (Appendix C1) with the Cl-content profile near the open interface. At $t = t_{degas}$, the boundary condition was removed in order to simulate the disappearance of the bubble-melt interface (namely, welding occurred), and the diffusive homogenization was then calculated until $t = t_{degas} + t_{postweld}$. Dt_{degas} and $Dt_{postweld}$ were determined such that the calculation profile best fits the observed data.

Acknowledgments
The authors thank Takeshi Kuritani for his constructive comments. Yoshimura thanks Jonathan Fink and Martin Streck for the discussion in Portland. Comments by Official Reviewers Iona McIntosh and Mattia Pistone, Associate Editor Luca Caricchi, and Editor Yves Bernabé, were helpful to improve the manuscript. Technical officers Hidehiko Nomura and Kosuke Nakamura prepared thin sections of excellent quality. This study was supported by JSPS Grant-in-Aid for Scientific Research (17K14376 and 20H01989) to Yoshimura and MEXT Kazan-PJ.

Data Availability Statement

All Cl and H_2O data used in this study are archived at http://dx.doi.org/10.17632/mvwzr6cxnw.1

References

Aiuppa, A., Baker, D. R., & Webster, J. D. (2009). Halogens in volcanic systems. *Chemical Geology*, *263*, 1–18. https://doi.org/10.1016/j.chemgeo.2008.10.005

Ban, M., Takahashi, K., Horie, T., & Toya, N. (2005). Petrogenesis of mafic inclusions in rhyolitic lavas from Narugo volcano, Northeastern Japan. *Journal of Petrology*, *46*, 1543–1563. https://doi.org/10.1093/petrology/egi025

Baxter, P. J., Banadonna, C., Dupree, R., Hards, V. L., Kohn, S. C., Murphy, M. D., et al. (1999). Cristobalite in volcanic ash of the Soufriere Hills Volcano, Montserrat, British West Indies. *Science*, *283*, 142–145. https://doi.org/10.1126/science.283.5405.1142

Berlo, K., Tuffen, H., Smith, V. C., Castro, J. M., Pyle, D. M., Mather, T. A., & Geraki, K. (2013). Element variations in rhyolitic magma resulting from gas transport. *Geochimica et Cosmochimica Acta*, *121*, 436–451. https://doi.org/10.1016/j.gca.2013.07.032

Boudon, G., Balcone-Boissard, H., Villemant, B., & Morgan, D. J. (2015). What factors control superficial lava dome explosivity? *Scientific Reports*, *5*, 14551. https://doi.org/10.1038/srep14551

Cabrera, A., Weinberg, R. F., Wright, H. M. N., Zlotnik, S., & Cas, R. A. F. (2011). Melt fracturing and healing: A mechanism for degassing and origin of silicic obsidian. *Geology*, *39*, 67–70. https://doi.org/10.1130/g31355.1

Castro, J. M., Bindeman, I. N., Tuffen, H., & Ian Schipper, C. (2014). Explosive origin of silicic lava: Textural and δD-H_2O evidence for pyroclastic degassing during rhyolite effusion. *Earth and Planetary Science Letters*, *405*, 52–61. https://doi.org/10.1016/j.epsl.2014.08.012

Castro, J. M., Cashman, K., Joslin, N., & Olmsted, B. (2002). Structural origin of large gas cavities in the Big Obsidian Flow, Newberry Volcano. *Journal of Volcanology and Geothermal Research*, *114*, 313–330. https://doi.org/10.1016/s0377-0273(01)00296-7

Castro, J. M., Cordonnier, B., Tuffen, H., Tobin, M. J., Puskar, L., Martin, M. C., & Bechtel, H. A. (2012). The role of melt-fracture degassing in defusing explosive rhyolite eruptions at volcán Chaitén. *Earth and Planetary Science Letters*, *333–334*, 63–69. https://doi.org/10.1016/j.epsl.2012.04.024

Castro, J. M., Manga, M., & Martin, M. C. (2005). Vesiculation rates of obsidian domes inferred from H_2O concentration profiles. *Geophysical Research Letters*, *32*, L21307. https://doi.org/10.1029/2005gl024029

Christopher, T., Edmonds, M., Humphreys, M. C. S., & Herd, R. A. (2010). Volcanic gas emissions from Soufrie`re Hills Volcano, Montserrat 1995–2009, with implications for mafic magma supply and degassing. *Geophysical Research Letters*, *37*, L00E04. https://doi.org/10.1029/2009gl041325

Crank, J. (1975). *The mathematics of diffusion* (p. 414). Oxford University Press.

de Hoog, J. C. M., van Bergen, M. J., & Jacobs, M. H. G. (2005). Vapour-phase crystallisation of silica from SiF4-bearing volcanic gases. *Annals of Geophysics*, *48*, 775–785.

Duan, X. (2014). A general model for predicting the solubility behavior of H_2O-CO_2 fluids in silicate melts over a wide range of pressure, temperature and compositions. *Geochimica et Cosmochimica Acta*, *125*, 582–609. https://doi.org/10.1016/j.gca.2013.10.018

Duan, Z., & Zhang, Z. (2006). Equation of state of the H_2O, CO_2, and H_2O-CO_2 systems up to 10 GPa and 2573.15K: Molecular dynamics simulations with ab initio potential surface. *Geochimica et Cosmochimica Acta*, *70*, 2311–2324. https://doi.org/10.1016/j.gca.2006.02.009

Edmonds, M. (2008). New geochemical insights into volcanic degassing. *Philosophical Transactions of the Royal Society A*, *366*, 4559–4579. https://doi.org/10.1098/rsta.2008.0185

Eichelberger, J. C., Carrigan, C. R., Westrich, H. R., & Price, R. H. (1986). Non-explosive silicic volcanism. *Nature*, *323*, 598–602. https://doi.org/10.1038/323598a0

Feisel, Y., Castro, J. M., & Dingwell, D. B. (2019). Diffusion of F and Cl in dry rhyodacitic melt. *American Mineralogist*, *104*, 1689–1699. https://doi.org/10.2138/am-2019-7095

Fink, J. H. (1983). Structure and emplacement of a rhyolitic obsidian flow: Little Glass Mountain, Medicine Lake Highland, northern California. *Geological Society of America Bulletin*, *94*, 362–380. https://doi.org/10.1130/0016-7606(1983)94<362:saeoar>2.0.co;2

Fink, J. H., Anderson, S. W., & Manley, C. R. (1992). Textural constraints on effusive silicic volcanism: Beyond the permeable foam model. *Journal of Geophysical Research*, *97*(B6), 9073–9083. https://doi.org/10.1029/92jb00416

Fink, J. H., & Kieffer, S. W. (1993). Estimate of pyroclastic flow velocities resulting from explosive decompression of lava domes. *Nature*, *363*, 612–615. https://doi.org/10.1038/363612a0

Fink, J. H., & Manley, C. R. (1987). Origin of pumiceous and glassy textures in rhyolite flows and domes (Vol. 212, pp. 77–88). Geological Society of America Special Paper.

Fortin, M.-A., Watson, E. B., & Stern, R. (2017). The isotope mass effect on chlorine diffusion in dacite melt, with implications for fractionation during bubble growth. *Earth and Planetary Science Letters*, *480*, 15–24. https://doi.org/10.1016/j.epsl.2017.09.042

Gardner, J. E., Burgisser, A., Hort, M., & Rutherford, M. (2006). Experimental and model constraints on degassing of magma during ascent and eruption (Vol. 402, pp. 85–99). Geological Society of America Special Paper.

Gardner, J. E., Llewellin, E. W., Watkins, J. M., & Befus, K. S. (2017). Formation of obsidian pyroclasts by sintering of ash particles in the volcanic conduit. *Earth and Planetary Science Letters*, *459*, 252–263. https://doi.org/10.1016/j.epsl.2016.11.037

Gardner, J. E., Wadsworth, F. B., Llewellin, E. W., Watkins, J. M., & Coumans, J. P. (2018). Experimental sintering of ash at conduit conditions and implications for the longevity of tuffisites. *Bulletin of Volcanology*, *80*, 33. https://doi.org/10.1007/s00445-018-1202-8

Gardner, J. E., Wadsworth, F. B., Llowellin, E. W., Watkins, J. M., & Coumans, J. P. (2019). Experimental constraints on the textures and origin of obsidian pyroclasts. *Bulletin of Volcanology*, *81*, 22. https://doi.org/10.1007/s00445-019-1283-z

Giordano, D., Russell, J. K., & Dingwell, D. B. (2008). Viscosity of magmatic liquids: A model. *Earth and Planetary Science Letters*, *271*, 123–134. https://doi.org/10.1016/j.epsl.2008.03.038

Gonnermann, H. M., & Manga, M. (2003). Explosive volcanism may not be an inevitable consequence of magma fragmentation. *Nature*, *426*, 432–435. https://doi.org/10.1038/nature02138

Gonnermann, H. M., & Manga, M. (2007). The fluid mechanics inside a volcano. *Annual Review of Fluid Mechanics*, *39*, 321–356. https://doi.org/10.1146/annurev.fluid.39.050905.110207

Heap, M. J., Tuffen, H., Wadsworth, F. B., Reuschlé, T., Castro, J. M., & Schipper, C. I. (2019). The permeability evolution of tuffisites and implications for outgassing through dense rhyolitic magma. *Journal of Geophysical Research: Solid Earth*, *124*, 8281–8299. https://doi.org/10.1029/2018JB017035

Holland, A. S. P., Watson, I. M., Phillips, J. C., Caricchi, L., & Dalton, M. P. (2011). Degassing processes during lava dome growth: Insights from Santiaguito lava dome, Guatemala. *Journal of Volcanology and Geothermal Research*, *202*, 153–166. https://doi.org/10.1016/j.jvolgeores.2011.02.004

Horwell, C. J., Hillman, S. E., Cole, P. D., Loughlin, S. C., Llewellin, E. W., Damby, D. E., & Crhistopher, T. E. (2014). Controls on variations in cristobalite abundance in ash generated by the Soufriere Hills Volcano, Montserrat in the period 1991 to 2010. In G. Wadge, R. E. A. Robertson, & B. Voight (Eds.), The eruption of Soufrière Hills volcano, Montserrat from 2000 to 2010 (Vol. 39, pp. 339–406). Geological Society.

Horwell, C. J., Le Blond, J. S., Michnowicz, S. A. K., & Cressey, G. (2010). Cristobalite in a rhyolitic lava dome: Evolution of ash hazard. *Bulletin of Volcanology*, *72*, 249–253. https://doi.org/10.1007/s00445-009-0327-1

Horwell, C. J., Williamson, B. J., Llewellin, E. W., Damby, D. E., & Le Blond, J. S. (2013). The nature and formation of cristobalite at the Soufrière Hills volcano, Montserrat: Implications for the petrology and stability of silicic lava domes. *Bulletin of Volcanology*, *75*, 696. https://doi.org/10.1007/s00445-013-0696-3

Kushnir, A. R. L., Martel, C., Champallier, R., & Arbaret, L. (2017). In situ confirmation of permeability development in shearing bubble-bearing melts and implications for volcanic outgassing. *Earth and Planetary Science Letters*, *458*, 315–326. https://doi.org/10.1016/j.epsl.2016.10.053

Liu, Y., Zhang, Y., & Behrens, H. (2005). Solubility of H_2O in rhyolitic melts at low pressures and a new empirical model for mixed H_2O-CO_2 solubility in rhyolitic melts. *Journal of Volcanology and Geothermal Research*, *143*, 219–235. https://doi.org/10.1016/j.jvolgeores.2004.09.019

Lukanin, O. A. (2015). Chlorine partitioning between melt and aqueous chloride fluid during granite magma. Degassing I. Decompression-induced melt degassing. *Geochemistry International*, *53*, 786–810. https://doi.org/10.1134/s0016702915090049

McIntosh, I. M., Llewellin, E. W., Humphreys, M. C. S., Nichols, A. R. L., Burgisser, A., Schipper, C. I., & Larsen, J. F. (2014). Distribution of dissolved water in magmatic glass records growth and resorption of bubbles. *Earth and Planetary Science Letters*, *401*, 1–11. https://doi.org/10.1016/j.epsl.2014.05.037

McIntosh, I. M., Nichols, A. R. L., Tani, K., & Llewellin, E. W. (2017). Accounting for the species-dependence of the 3500 cm^{-1} H_2O_t infrared molar absorptivity coefficient: Implications for hydrated volcanic glasses. *American Mineralogist*, *102*, 1677–1689. https://doi.org/10.2138/am-2017-5952ccby

Nakamura, M., Otaki, K., & Takeuchi, S. (2008). Permeability and pore-connectivity variation of pumices from a single pyroclastic flow eruption: Implications for partial fragmentation. *Journal of Volcanology and Geothermal Research*, *176*, 302–314. https://doi.org/10.1016/j.jvolgeores.2008.04.011

Navon, O., Chekhmir, A., & Lyakhovsky, V. (1998). Bubble growth in highly viscous melts: Theory, experiments, and autoexplosivity of dome lavas. *Earth and Planetary Science Letters*, *160*, 763–776. https://doi.org/10.1016/s0012-821x(98)00126-5

Newman, S., Stolper, E. M., & Epstein, S. (1986). Measurement of water in rhyolitic glasses: Calibration of an infrared spectroscopic technique. *American Mineralogist*, *71*, 1527–1541.

Okumura, S., Nakamura, M., Nakano, T., Uesugi, K., & Tsuchiyama, A. (2010). Shear deformation experiments on vesicular rhyolite: Implications for brittle fracturing, degassing, and compaction of magmas in volcanic conduits. *Journal of Geophysical Research*, *115*, B06201. https://doi.org/10.1029/2009JB006904

Okumura, S., Nakamura, M., & Nakashima, S. (2004). Determination of molar absorptivity of IR fundamental OH-stretching vibration in rhyolitic glasses. *American Mineralogist*, *88*, 1657–1662.

Okumura, S., Nakamura, M., Uesugi, K., Nakano, T., & Fujioka, T. (2013). Coupled effect of magma degassing and rheology on silicic volcanism. *Earth and Planetary Science Letters*, *362*, 163–170. https://doi.org/10.1016/j.epsl.2012.11.056

Omoto, K. (1993). Radiocarbon ages of organic materials collected from Naruko Basin, Miyagi prefecture. *Daiyonki Kenkyu*, *32*, 227–229. https://doi.org/10.4116/jaqua.32.227

Paisley, R., Berlo, K., Whattam, J., Schipper, C. I., & Tuffen, H. (2019). Degassing-induced chemical heterogeneity at the 2011–2012 Cordón Caulle eruption. *Volcanica*, *2*, 211. https://doi.org/10.30909/vol.02.02.211237

Prousevitch, A. A., & Sahagian, D. L. (1996). Dynamics of coupled diffusive and decompressive bubble growth in magmatic systems. *Journal of Geophysical Research*, *101*, 17447–17455. https://doi.org/10.1029/96JB01342

Quane, S. L., & Russell, J. K. (2005). Welding: Insights from high-temperature analogue experiments. *Journal of Volcanology and Geothermal Research*, *142*, 67–87. https://doi.org/10.1016/j.jvolgeores.2004.10.014

Rust, A. C., & Cashman, K. V. (2007). Multiple origins of obsidian pyroclasts and implications for changes in the dynamics of the 1300 B.P. eruption of Newberry volcano, USA. *Bulletin of Volcanology*, *69*, 825–845. https://doi.org/10.1007/s00445-006-0111-4

Sato, H., Fujii, T., & Nakada, S. (1992). Crumbling of dacite dome lava and generation of pyroclastic flows at Unzen volcano. *Nature*, *360*, 664–666. https://doi.org/10.1038/360664a0

Saubin, E., Tuffen, H., Gurioli, L., Owen, J., Castro, J. M., Berlo, K., et al. (2016). Conduit dynamics in transitional rhyolitic activity recorded by tuffisite vein textures from the 2008-2009 Chaitén eruption. *Frontiers of Earth Science*, *4*, 59. https://doi.org/10.3389/feart.2016.00059

Schipper, C. I., Castro, J. M., Tuffen, H., James, M. R., & How, P. (2013). Shallow vent architecture during hybrid explosive-effusive activity at Cordón Caulle (Chile, 2011-12): Evidence from direct observations and pyroclast textures. *Journal of Volcanology and Geothermal Research*, *262*, 25–37. https://doi.org/10.1016/j.jvolgeores.2013.06.005

Schipper, C. I., Castro, J. M., Tuffen, H., Wadsworth, F. B., Chappell, D., Pantoja, A. E., et al. (2015). Cristobalite in the 2011-2012 Cordón Caulle eruption (Chile). *Bulletin of Volcanology*, *77*, 34. https://doi.org/10.1007/s00445-015-0925-z

Schipper, C. I., Mandon, C., Maksimenko, A., Castro, J. M., Conway, C. E., Hauer, P., et al. (2017). Vapor-phase cristobalite as a durable indicator of magmatic pore structure and halogen degassing: An example from White Island volcano (New Zealand). *Bulletin of Volcanology*, *73*, 4. https://doi.org/10.1007/s00445-017-1157-1

Shinohara, H. (2009). A missing link between volcanic degassing and experimental studies on chloride partitioning. *Chemical Geology*, *263*, 51–59. https://doi.org/10.1016/j.chemgeo.2008.12.001

Stasiuk, M. V., Barclay, J., Carroll, M. R., Jaupart, C., Ratté, J. C., Sparks, R. S. J., & Tait, S. R. (1996). Degassing during magma ascent in the Mule Creek vent (USA). *Bulletin of Volcanology*, *58*, 117–130. https://doi.org/10.1007/s004450050130

Tsuchiya, N., Ito, J., Seki, Y., & Iwaya, T. (1997). *Geology of the Iwagasaki district*. Geological Survey of Japan.

Tuffen, H., & Dingwell, D. (2005). Fault textures in volcanic conduits: Evidence for seismic trigger mechanisms during silicic eruptions. *Bulletin of Volcanology*, *67*, 370–387. https://doi.org/10.1007/s00445-004-0383-5

Tuffen, H., Dingwell, D. B., & Pinkerton, H. (2003). Repeated fracture and healing of silicic magma generate flow banding and earthquakes? *Geolology*, *31*, 1089–1092. https://doi.org/10.1130/g19777.1

Tuffen, H., Smith, R., & Sammonds, P. R. (2008). Evidence for seismogenic fracture of silicic magma. *Nature*, *453*, 511–514. https://doi.org/10.1038/nature06989

Villemant, B., & Boudon, G. (1998). Transition from dome-forming to plinian eruptive styles controlled by H_2O and Cl degassing. *Nature*, *392*, 65–69. https://doi.org/10.1038/32144

Villemant, B., & Boudon, G. (1999). H_2O and halogen (F, Cl, Br) behavior during shallow magma degassing processes. *Earth and Planetary Science Letters*, *168*, 271–286. https://doi.org/10.1016/s0012-821x(99)00058-8

von Aulock, F. W., Kennedy, B. M., Maksimenko, A., Wadsworth, F. B., & Lavallée, Y. (2017). Outgassing from open and closed magma foams. *Frontiers of Earth Science*, *5*, 46. https://doi.org/10.3389/feart.2017.00046

Watkins, J. M., Gardner, J. E., & Befus, K. S. (2017). Nonequilibrium degassing, regassing, and vapor fluxing in magmatic feeder systems. *Geology*, *45*, 183–186. https://doi.org/10.1130/g38501.1

Watkins, J. M., Manga, M., & DePaolo, D. J. (2012). Bubble geobarometry: A record of pressure changes, degassing, and regassing at Mono Craters, California. *Geology*, *40*, 699–702. https://doi.org/10.1130/g33027.1

Watson, E. B. (1991). Diffusion of dissolved CO_2 and Cl in hydrous silicic to intermediate magmas. *Geochimica et Cosmochimica Acta*, *55*, 1897–1902.

Watson, E. B. (2017). Diffusive fractionation of volatiles and their isotopes during bubble growth in magmas. *Contributions to Mineralogy and Petrology*, *172*, 61. https://doi.org/10.1007/s00410-017-1384-7

Webster, J. D., & Holloway, J. R. (1988). Experimental constraints on the partitioning of Cl between topaz rhyolite melt and H_2O and H_2O + CO_2 fluids: New implications for granitic differentiation and ore deposition. *Geochimica et Cosmochimica Acta*, *52*, 2091–2105. https://doi.org/10.1016/0016-7037(88)90189-5

Westrich, H. R., & Eichelberger, J. C. (1994). Gas transport and bubble collapse in rhyolitic magma: An experimental approach. *Bulletin of Volcanology*, *56*, 447–458. https://doi.org/10.1007/s004450050054

Yoshimura, S. (2018). Chlorine diffusion in rhyolite under low-H_2O conditions. *Chemical Geology*, *483*, 619–630.

Yoshimura, S., Kuritani, T., Matsumoto, A., & Nakagawa, M. (2019). Fingerprint of silicic magma degassing visualized through chlorine microscopy. *Scientific Report*, *9*, 786. https://doi.org/10.1038/s41598-018-37374-0

Yoshimura, S., & Nakamura, M. (2008). Diffusive dehydration and bubble resorption during open-system degassing of rhyolitic melts. *Journal of Volcanology and Geothermal Research*, *178*, 78–80. https://doi.org/10.1016/j.jvolgeores.2008.01.017

Yoshimura, S., & Nakamura, M. (2010). Fracture healing in a magma: An experimental approach and implications for volcanic seismicity and degassing. *Journal of Geophysical Research*, *115*, B09209. https://doi.org/10.1029/2009JB000832

Zhang, Y., & Ni, H. (2010). *Diffusion of H, C, and O components in silicate melts*. In Y. Zhang, & D. J. Cherniak (Eds.), Diffusion in minerals and melts. Reviews in mineralogy and geochemistry (Vol. 72, pp. 171–225). Mineralogical Society of America.